Astronomy & Astrophysics manuscript no. DanutaParaficz˙arxiv
May 17, 2016
© ESO 2016

The PCA Lens-Finder: application to CFHTLS

D. Paraficz[1], F. Courbin[1], A. Tramacere[2], R. Joseph[1], R.B. Metcalf[3], J.-P. Kneib[1], P. Dubath[2], D. Droz[1], F. Filleul[1], D. Ringeisen[1], C. Schäfer[1]

[1] Laboratoire d'Astrophysique Ecole Polytechnique Fédérale de Lausanne (EPFL) Observatoire de Sauverny CH-1290 Versoix
[2] Department of Astronomy, University of Geneva, Ch. d'Écogia 16, CH-1290 Versoix, Switzerland
[3] Dipartimento di Fisica e Astronomia - Universita di Bologna, via Berti Pichat 6/2, 40127, Bologna, Italy

May 17, 2016

arXiv:1605.04309v1 [astro-ph.GA] 13 May 2016

ABSTRACT

We present the results of a new search for galaxy-scale strong lensing systems in CFHTLS *Wide*. Our lens-finding technique involves a preselection of potential lens galaxies, applying simple cuts in size and magnitude. We then perform a Principal Component Analysis of the galaxy images, ensuring a clean removal of the light profile. Lensed features are searched for in the residual images using the clustering topometric algorithm DBSCAN. We find 1098 lens candidates that we inspect visually, leading to a cleaned sample of 109 new lens candidates. Using realistic image simulations we estimate the completeness of our sample and show that it is independent of source surface brightness, Einstein ring size (image separation) or lens redshift. We compare the properties of our sample to previous lens searches in CFHTLS. Including the present search, the total number of lenses found in CFHTLS amounts to 678, which corresponds to ∼4 lenses per square degree down to $i(AB) = 24.8$. This is equivalent to ∼ 60.000 lenses in total in a survey as wide as Euclid, but at the CFHTLS resolution and depth.

Key words. gravitational lensing, galaxies, surveys

1. Introduction

Strong gravitational lensing occurs when light rays emitted by a distant source are deflected by the potential well of a foreground mass (Einstein 1916). If the latter is compact enough i.e. above the lensing critical surface mass density, multiple images of the background source are formed. Because strong lensing has only simple dependence on its geometry and fundamental physics (general relativity), thus its applications in cosmology and in the study of galaxy formation and evolution are straightforward and becoming more and more numerous.

Strong gravitational systems have been used in recent years to address key scientific questions. In particular, strong lensing consists of a powerful tool to map the total mass (dark and luminous) in galaxies, independently of their dynamical state or star formation history (e.g. Treu et al. 2002; Rusin et al. 2003; Treu & Koopmans 2004; Rusin & Kochanek 2005; Sonnenfeld et al. 2012; Bolton et al. 2012). Also, thanks to strong lensing, small and dark satellite galaxies have even been found and weighted (e.g. Metcalf & Madau 2001; Dalal & Kochanek 2002; Treu & Koopmans 2004; Koopmans et al. 2006; Jiang & Kochanek 2007; Gavazzi et al. 2007; Treu et al. 2010; Auger et al. 2010; Bolton et al. 2012; Sonnenfeld et al. 2012; Vegetti et al. 2012; Oguri et al. 2014). Applications in cosmology using the time delay method (e.g. Refsdal 1964) between the multiply-lensed images of distant quasars are also becoming of increasing interest thanks to intensive photometric monitoring programs like COSMOGRAIL (e.g. Vuissoz et al. 2008; Courbin et al. 2011; Rathna Kumar et al. 2013; Tewes et al. 2013). In combination with state-of-the-art modelling tools, these time delays can be used to constrain the cosmological parameters both with precision and accuracy (e.g. Suyu 2012; Suyu et al. 2010, 2013, 2014). Even without time delay measurements, large samples of galaxy-scale strong lenses can help to constrain cosmology, as Cao et al. (2015) did, using 118 systems to constrain the dark energy equation of state parameter, w.

The above applications of strong lensing are possible because: 1. significantly large samples of strong lensing systems are now available, 2. some of the discovered systems have specific, rare properties making them particularly effective in delivering astrophysical or cosmological constraints. The ongoing (DES, KIDS) and planned wide field surveys of the next decade (Euclid, LSST, WFIRST) will continue to revolutionise the field, by making available hundreds of thousands of new strong lenses (e.g. Pawase et al. 2014; Collett 2015), i.e. ∼3 orders of magnitude larger than the current sample sizes.

Early systematic searches for strong lenses took advantage of the so-called lensing magnification bias, i.e. the fact that a lensed source is seen brighter because it is lensed. These source-selected lensing system samples were built by looking for multiple images among samples of optically bright quasars (e.g. Surdej et al. 1987; Magain et al. 1988). This was followed up in a more systematic way with a search in the Hamburg-ESO bright quasar catalogue (Wisotzki et al. 1993, 1996, 1999, 2002, 2004; Blackburne et al. 2008), in the SDSS with the Sloan Quasar Lens Survey (SQLS; Inada et al. 2003, 2012; Oguri et al. 2006, 2008; Inada et al. 2007) as well as in other wide-field optical observations (e.g. Winn et al. 2000, 2001, 2002b,a). Similarly, strong lens searches were also carried out in the radio in the FIRST survey (Gregg et al. 2000) and in the CLASS survey (Myers et al. 2003; Browne et al. 2003). More recently, the same strategy was adopted at millimeter wavelengths with the South Pole Telescope (SPT Hezaveh et al. 2013), and at sub-millimeter wavelengths with the Herschel satellite like H-ATLAS (Negrello et al. 2010; González-Nuevo et al. 2012; Bussmann et al. 2013) and HerMES (Conley et al. 2011; Gavazzi et al. 2011; Wardlow et al. 2013).

Source-selected samples of lensing systems are mostly composed of lensed quasars. Searches for non-quasar lensed galaxies are generally carried out by preselecting a sample of potential lensing galaxies and by looking for lensed images or spectra in their background (Ratnatunga et al. 1999; Fassnacht et al. 2004; Moustakas et al. 2007; Cabanac et al. 2007; Belokurov et al. 2007; Faure et al. 2008; Marshall et al. 2009; Pawase et al. 2014; More et al. 2016). These lens-selected samples are best constructed using spectra where sets of emission lines at two (or more) distinct redshifts are looked for. The method was pioneered by (Willis et al. 2005, 2006) with their Optimal Line-of-Sight Survey, soon followed by the SloanLens ACS Survey (SLACS, e.g., Bolton et al. 2006; Treu et al. 2006; Koopmans et al. 2006; Gavazzi et al. 2007, 2008; Bolton et al. 2008; Auger et al. 2009) and by the BOSS Emission-Line Lens Survey (BELLS; Brownstein et al. 2012). The SLACS sample on its own has about 100 confirmed gravitational lenses in the redshift range $0.1 < z < 0.4$ with HST imaging (e.g. Bolton et al. 2006; Auger et al. 2009). The main advantage of the spectroscopic approach is that the redshifts of the lens and of the source are readily obtained, along with the stellar velocity dispersion in the lens (e.g. Treu & Koopmans 2004; Koopmans et al. 2006; Auger et al. 2010). Moreover, if the source has strong emission lines, then the light from the lens and the source can easily be separated.

In the imaging, on the other hand, the source is often hidden in the lens glare, thus it cannot be detected so easily. For this reason carrying out an imaging lens search requires careful image processing to efficiently remove the lens light and unveil any faint background lensed galaxy. Such techniques start to be implemented, and will become increasingly important with the development of large sky surveys like DES, KIDS, Euclid, the LSST and WFIRST.

Based on two-band imaging, Gavazzi et al. (2014) have devised a method to detect faint blue arcs behind foreground redder galaxies. They extend their technique to multi-band lens modelling (Brault & Gavazzi 2015) and they apply them to the CFHTLS (Canada-France-Hawaii Telescope Legacy Survey) data (Cuillandre et al. 2012). A second method was introduced by Joseph et al. (2014) that can work both in single-band and multi-band. It is based on a principal component analysis (PCA; Jolliffe 1986) of the full imaging dataset to subtract the image of galaxies, even in the presence of complex structures. The residual image can then be used to search for lensed sources. In this paper, we use the method of Joseph et al. (2014) to extend the sample of known galaxy-scale strong lenses in CFHTLS.

The paper is organized as follows. In Sect. 2, we provide a brief description of the observational material and of the sample selection technique from the object catalogues for the CFHTLS. In Sect. 3, we describe the lens-finding algorithm based on PCA and its improvements. In Sect. 4, we present the list of our new lens candidates and compare it to previous results from other lens searches in the same area of sky, i.e., the CFHTLS fields. In Sect. 5, we discuss the completeness of the sample based on lens simulation. Finally, in Sect. 6, we provide a summary of the main conclusions from this work and provide a short outlook for future progress.

Throughout this work, we assume $\Omega_0 = 0.3$, $\Omega_\Lambda = 0.7$, and $H_0 = 70$ kms^{-1}Mpc^{-1}. All magnitudes are in the AB system (Oke & Gunn 1983).

2. Observational material and sample selection

Our main goal in this work is to complement and extend current samples of galaxy-scale strong lens candidates, starting with the public imaging data from the CFHTLS. To do so, we use the new technique proposed by Joseph et al. (2014).

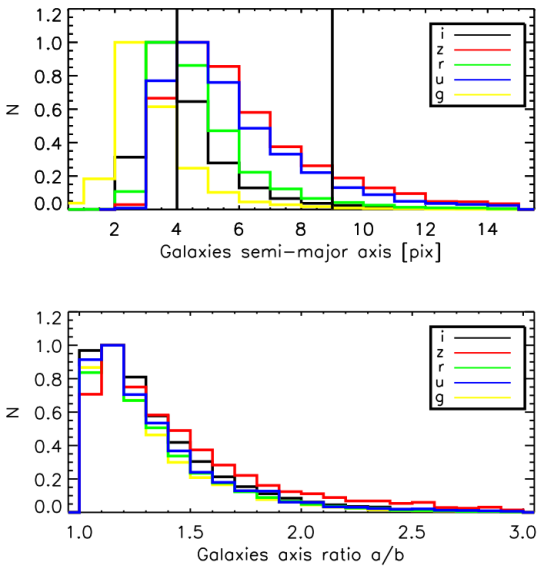

Fig. 1. Distribution of the semi-major axes and of their ratio, for our preselections of galaxies in the full CFHTLS sample (Cuillandre et al. 2012). The vertical lines mark our size cut-off of galaxies. The pixel size is 0.″187.

2.1. CFHTLS data

The Canada-France-Hawaii-Telescope Legacy Survey is a large program consisting of 500 observing nights between January 2003 and early 2009, divided into two parts. The *Deep* survey has 4 ultra-deep pointings and the *Wide* survey has 171 intermediate-depth pointings. Because strong lensing systems are rare, we need to use the widest possible survey area, i.e. the *Wide* part of CFHTLS.

The *Wide* CFHTLS (Cuillandre et al. 2012) covers 155 deg^2 divided into four independent fields observed in five bands. The limiting point-source AB magnitude (80% completeness) for each band is $u = 25.2$, $g = 25.5$, $r = 25.0$, $i = 24.8$, $z = 23.9$. For each band the mean seeing is FWHM= 0.″85, 0.″79, 0.″71, 0.″64, and 0.″68, respectively. The pixel size of the CFHTLS data is 0.″187.

In this paper, we use the T0007[1] final release of the CFHTLS with improved flat-fielding and photometric calibration techniques developed by the Supernova Legacy Survey (SNLS) team in collaboration with the CFHT. This release benefits from two types of photometric catalogues: 1. source catalogues for individual images (i.e. the `.ldac` files in the T0007 package) that we use to build our samples of lens galaxies in each filter separately, 2. merged source catalogues produced from the *g*, *r*, and *i* images that we use to infer the colour information of our lenses. The full description of the CFHTLS-T0007 release can be found in Cuillandre et al. (2012).

[1] See details at http://www.cfht.hawaii.edu/Science/CFHLS/

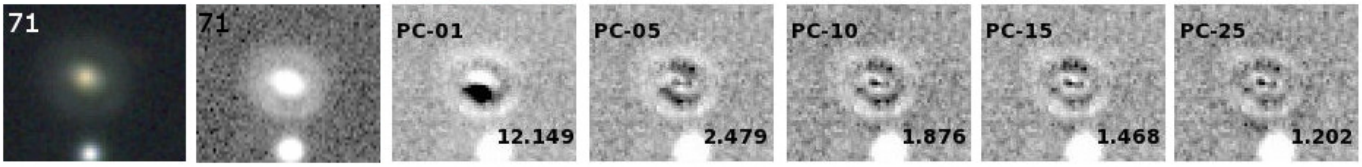

Fig. 2. Illustration of the PCA reconstruction of a galaxy image. The first two panels show the original image (colour and single-band). Each of the other panels shows the residual image between the data and the reconstructed galaxy using respectively 1, 5, 10, 15 and 25 principal components (PCs). The value of the corresponding reduced χ^2 is given in the lower right corner.

2.2. Sample selection

We preselect galaxies among the full CFHTLS source catalogues for individual images produced by TERAPIX using SEXTRACTOR (Bertin & Arnouts 1996). PCA requires uniform in size, morphology and brightness sample of elliptical galaxies, and since size and morphology of a galaxy changes between different bands, thus we create five catalogues, one for each of the five CFHTLS filters, independently. A given galaxy can therefore appear in several of the catalogues. Before using the PCA subtraction technique of Joseph et al. (2014), we apply the following selection criteria to each of the five catalogues:

- We use only the objects classified as non-stellar by SEXTRACTOR (CLASS_STAR > 0.98) and we apply a detection threshold of 10σ for each band, that is $u = 23.9$, $g = 24.3$, $r = 23.5$, $i = 23.5$, $z = 22.4$. Fainter objects would make difficult targets for future spectroscopic follow-up.
- We apply a cut on the semi-axis ratio, $a/b < 3$, which includes most of the early-type galaxies (Park et al. 2007), but rejects most of the spurious objects like those "created" by diffraction patterns of bright stars.
- We apply an (angular) size cut-off. Small galaxies, with a semi-major axis $a < 4$ pixels are excluded. Any arc in their vicinity can be detected without subtracting the light of the foreground galaxy. We also remove galaxies with $a > 9$ pixels. These galaxies are rare and therefore poorly modeled with the PCA technique (Joseph et al. 2014). Since we want to ensure uniformity of galaxy shapes in a group, galaxy sizes are computed separately in each band. Our final selection therefore spans sizes in the range $4 < a < 9$ pixels. Figure 1 displays the distribution in semi-major axis for the full sample in all the CFHTLS bands.

This leaves us with a pre-selection of early-type and late-type galaxies. However, spiral arms can be mistakenly taken for lensed arcs, resulting in false positives. To avoid this, we further restrict the sample to only elliptical galaxies. This can be achieved by either using a galaxy classifier based in morphological features in images (e.g. the `ASTErIsM` software by A. Tramancere, et al., 2015 submitted) or by applying a colour selection. We adopt the latter strategy, selecting galaxies with $(g - i) > 1.0$ within a $3''$ aperture, following Gavazzi et al. (2010). Obviously, some of the potential lenses are missed by this selection, but this is the price to pay to remove spiral galaxies efficiently.

For each selected object, we create an image stamp centred on the galaxy. Since rotation is not a principal component, we also apply a rotation to each stamp to align the major axes of all galaxies. In doing so, we use a polynomial transformation and a bilinear interpolation. We note that we do not apply any other re-scaling. Instead, to ensure final uniformity of the PCA basis, we take advantage of the very large sample and we split it in five bins of galaxies sizes. The five groups are defined by the galaxies semi-major axis as follows: (1): $a = [4 - 5]$, (2): $a = [5 - 6]$, (3): $a = [6 - 7]$, (4): $a = [7 - 8]$, and (5): $a = [8 - 9]$ pixels.

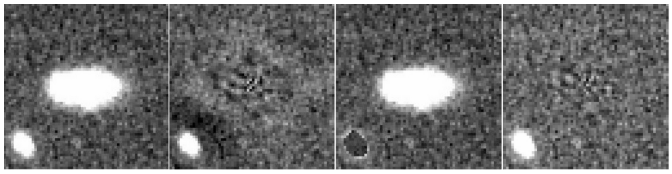

Fig. 3. Illustration of our masking strategy. *From left to right*: a) image of a galaxy from our sample, b) subtraction without using a mask during the reconstruction process, leaving ring-like artefacts, c) masked image used for the reconstruction process, d) resulting residual image, without any artefact.

3. Lens-finding algorithm and improvements

Our algorithm by nature finds bright lensing galaxies. In such samples the lensed source is often hidden in the glare of the foreground galaxy, which must be properly removed before any search for lensed structures can be carried out. Our PCA-based lens-finder therefore includes two steps: 1. subtraction of the central galaxy from the original images/stamps, using PCA image reconstruction and 2. detection of lensed extended objects (arcs, rings) in the residual images.

3.1. Removal of the lensing galaxy: the PCA approach

Traditional ways of subtracting galaxies in imaging data are either to fit a elliptical profile to the data with, for example, the `galfit` software (Peng et al. 2010; Cabanac et al. 2008) or to subtract aperture-scaled images in two different bands (Gavazzi et al. 2014). As galaxies are not perfect elliptical profiles, these approaches often leads to significant flux residuals that prevents the detection of faint background lensed objects and they produce large amounts of false positives.

Our solution to this problem is presented in Joseph et al. (2014) [2], where we build an empirical galaxy light model from the sample of galaxies itself using a principal component analysis. PCA decomposition of a dataset allows one to recognise any similarity among its elements: the elements in the dataset are converted into another set of variables called principal components (PC), which are orthogonal and ordered so that the first PC has the largest possible variance, the second PC has the second largest variance, and so on. The details of our PCA technique are provided in Joseph et al. (2014).

[2] PCA script available at `https://github.com/herjy/PiCARD`

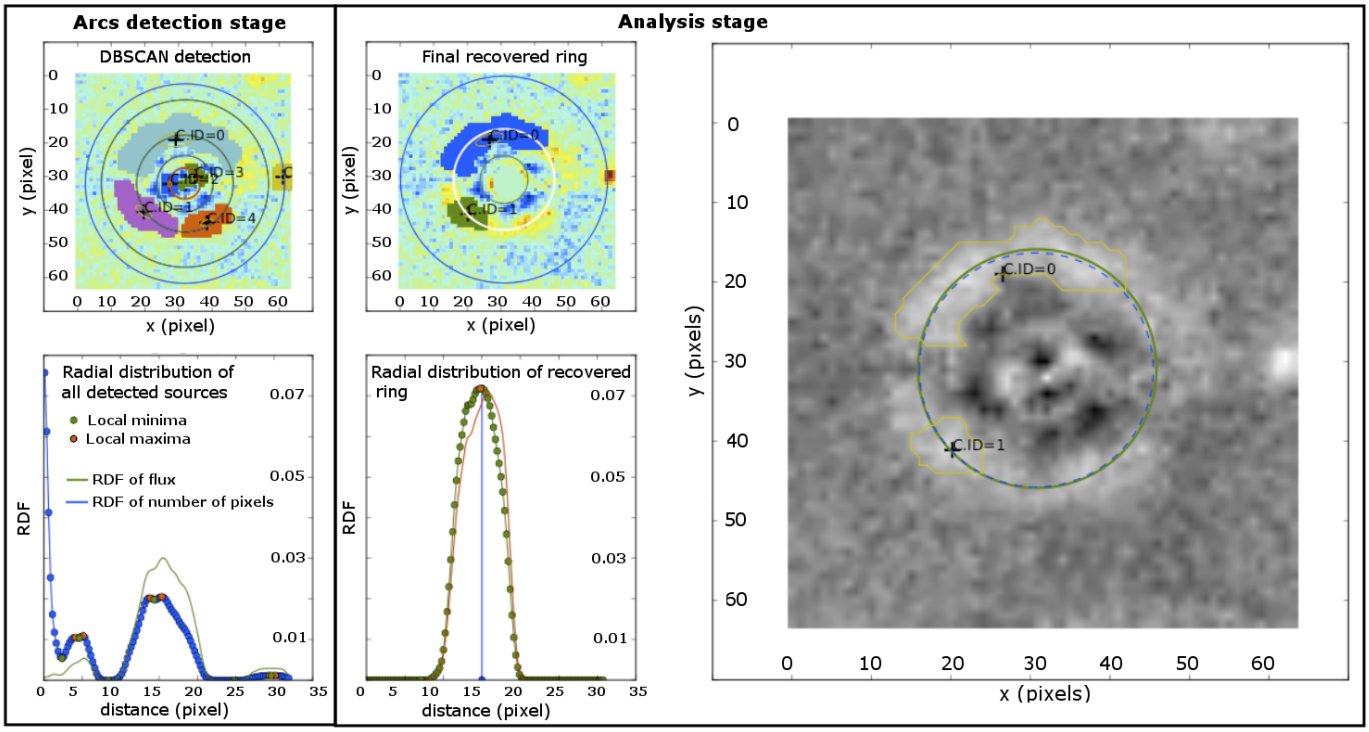

Fig. 4. Analysis of the PCA-subtracted images. **Arc detection stage.** *Top panel*: DBSCAN detection of the sources. *Bottom panel*: radial distribution of the detected sources. The green solid line represents the pixel flux radial distribution, while the blue line represents the radial distribution of the number of pixels in the sources. **Analysis stage.** *Top panel*: All sources smaller than a critical angular size (e.g. the PSF size) are removed, the remaining sources are merged together in the final ring (indicated with white line). *Bottom panel* The red solid line represents the pixel flux radial distribution, while the green line represents the radial distribution of the number of pixels in the sources. *Right panel*: Residual image, where the green solid line shows the best circle fit to the final ring. The yellow lines show the contour of the components of the final ring.

A critical step in the PCA reconstruction is the choice of the number of PC coefficients. If all coefficients are used, the reconstructed image is identical to the original image. This clearly leads to overfitting of the data and noise and will simply remove all structures of interest, like faint lensed rings and arcs. To circumvent this problem, the galaxy image needs to reconstructed using only a limited number of coefficients. Obviously, there might be an optimal number of coefficients to be used to avoid over-fitting or under-fitting of the data. This optimal number of PC depends on the diversity in shape among the galaxies in the sample, i.e. the range in galaxy sizes, the presence of companions near the galaxies used to build the PCA basis, and it also depends on the number of objects used to build the PCA basis. Fig. 2 gives an illustration of a galaxy image reconstructed from a different number of PCs. To evaluate the overall quality of reconstruction of a galaxy image in an objective way, we compute the reduced χ^2 in the image after subtraction of the galaxy (Eq. 6 in Joseph et al. 2014). An ideal reconstruction gives a reduced χ^2 close to one. Of course lensed features in the image do produce signal in the residual image, a cut-off in χ^2 has to be defined that ensures an adequate tradeoff between clean removal of the foreground galaxy and non-removal of any potential lensed feature. Finding this cut-off is a subjective part of our procedure and final result for false to true positives ratio will strongly depend on the adopted value. In the present case we choose $\chi^2 \sim 1.4$ for the CFHTLS data (see Fig. 2) and for the simulations used to evaluate completeness of the procedure (see Section 5).

The PCA technique described in Joseph et al. (2014) works well for isolated galaxies. In practice, however, galaxies often have companions, either physical or the result of line-of-sight effects. Companions affect the results both when building the PCA basis from the galaxy sample and when reconstructing the image of a given galaxy. The first problem (as described already in Joseph et al. 2014) is easily avoided by computing the PCA basis on a subset of galaxies with no bright companions. The large size of our galaxy sample allows us to do that in practice. However, companions are present in the images of the galaxy we want to reconstruct and subtract. In the case of reconstruction of an image of a galaxy with bright companions, residuals might feature artifacts that mimic a ring (Fig. 3). To avoid this problem we simply mask bright companion before the reconstruction process. Images reconstructed in this manner are then subtracted from original, non-masked images creating residuals that are now free of the false rings. Figure 3 illustrates the improvement over a non-masked image.

To apply the masking to all the companion sources in the image stamps, we use the DBSCAN algorithm implemented in the ASTErIsM software (Tramacere et al 2015 submitted). We identify the object at the centre of the stamp, as our source of interest that will be not masked. We iterate among all the remaining sources, and we mask all the sources with an integrated flux larger than the half of the central galaxy's integrated flux and all the sources with a distance from the central galaxy smaller than the half of the central galaxy's radius. The masked pixel fluxes are replaced with flux values randomly sampled from the background pixels flux distribution.

3.2. Looking for lensed features in the residual image

Once the galaxies have been properly removed from all preselected image stamps, we can now search for lensing features in these residual images. To avoid too many false positives we choose to search for only arc-like features. This was done using the cluster/island detection algorithm described in detail and tested in Tramacere et al (2015, in prep). Below, we provide a short overview of the procedure. This method is based on the application of the DBSCAN clustering topometric algorithm [3] (Easter et al. 1996; Tramacere & Vecchio 2013), which extracts *sources* in image stamps by defining density-based *clusters* of connected pixels. The method consists in the following two steps (see Fig. 4).

1. **Arcs and rings detection stage**
   - An initial list of sources is extracted using the DBSCAN algorithm (Top-left panel of Fig. 4);
   - The shape of each source is determined and each source is flagged to be: arc-like, ring-like, ellipse-like, circular/point-like;
   - All point-like sources are removed, leaving us with a list of candidate lensed sources;
   - For each stamp in the candidate list, we compute the radial distribution of the sources, and we determine the minima and the maxima in this radial distribution. This is presented on the bottom-left panel of Fig. 4, where the green filled circles represent the local minima, and the red filled circles represent the local maxima. The first minima in the innermost ring sets the radius for the internal disk, indicated as a red circle in the top-left panel of Fig. 4. These allow us to partition the stamps in circular areas.
   - All the sources within the internal disk (red circle in the left-top panel of Fig. 4) are masked, i.e. all the corresponding pixels are set to the background flux level (central-top panel of Fig. 4);
   - All the sources in the candidate list are assigned to a single circular area for each sources, enabling us to easily measure the angular size and the orientation of the sources, α_r, with regard to the radial direction;
   - All sources smaller than a critical angular size (e.g. the PSF size) are removed; only rings with at least one source meeting criteria are kept;
   - The sources are then merged together in the final ring to preform the analysis (see central panel in Fig. 4)

2. **Analysis stage**
   - Once we have a *final* ring, we fit a circle to the distribution of pixels in the recovered ring and we measure a centroid position, barycentre and radius, R (green circle in the left panel of Fig. 4).
   - We also fit a circle to each of the ring components that have an arc-like shape (blue dashed line in the right panel of Fig. 4), and we check that the circle is contained within the final ring best-fit circle.
   - We assign a quality factor to the ring, which is determined by the total angular coverage of the ring θ_{tot}, and the displacement d, between the ring circle best fit centroid, and the ring barycentre

$$q_f = \frac{\theta_{tot}}{2\pi} \frac{1}{\exp(\frac{d-R}{R/f}) + 1} \quad (1)$$

where the larger the value of f, the more conservative the quality factor is. In this work we adopt minimum $q_f = 0.1$ to flag an object that are a possible lens.

We apply this automated procedure to the five bands of CFHTLS imaging data after PCA subtraction of the foreground object, leading to 1 098 lens candidates passing all above criteria.

4. CFHTLS results

In the following, we describe our main results using the PCA-finder. This includes a visualisation step by five of the authors, allowing us to define three subsamples of lens candidates depending on how likely the candidates are to be real lenses. The characteristics of our new sample are compared with previous lens searches in the CFHTLS.

4.1. Visual inspection

The automatically selected 1 098 candidates were visually inspected to identify obvious spurious objects and to refine our lensing classification. We rank each object in one of the following categories:

- **A**: an almost definite lens with a striking image configuration that is typical for lensing;
- **B**: probable lens, but the candidate would need follow-up with spectroscopy or more imaging;
- **C**: possible lens, but with low probability of being confirmed, either because of low signal-to-noise (S/N) or because the potential lensed images are single or consist of short arcs that could still be compatible with edge-on galaxies or chain galaxies;
- **0**: not a lens, spurious detection or spiral galaxy mimicking an arc or an Einstein ring. Objects in this category are false-positives.

The visual classification is a time-consuming process. However, the workload remains reasonable in the case of the CFHTLS, which requires a few hours of human time to inspect the 1 098 candidates. The classification is performed both on the true-colour images using the g, r, and i bands and on the residual images. This is done using the FITS images, enabling us to easily and quickly explore the full dynamical range of the data. This classification is made independently by five of the authors: D.P., J.-P.K., R.J., F.C., P.D. Out of all the systems, we select those objects that are classified as definite lenses by at least one individual initial judgment. All authors then needed to agree on a final classification. Figures A.1-A.5 in the Appendix and Tables 1-2 present all the lens candidates that we rank with the grade *A* and grade *B*.

Our visual inspection shows that the most frequent contaminants are face-on spiral galaxies, ring galaxies and polar ring galaxies. Face-on spirals mistakenly taken by the PCA-finder as lens candidates are easily identified by eye because their spiral arms point towards the bulge, while lensed arcs are tangentially aligned with respect to their lens galaxy.

More problematic are ring-like galaxies in general and polar ring galaxies in particular. These rare composite galaxies consist of a gas-poor, early-type galaxy (typically S0 galaxies) surrounded by a blue gaseous ring with ongoing star formation (see Fig. 5). The most widely accepted explanation for the formation of polar ring galaxies is that accreted gas settles onto orbits

[3] DBSCAN algorithm available at a (Easter et al. 1996; Tramacere & Vecchio 2013)

ID	RA	DEC	z	$R_{\rm eff}$	g	r	i	$R_{\rm E}$	Quality
				pix	mag	mag	mag	pix	
1	30.2905	-6.3474	$0.548^{+0.587}_{-0.507}$	4.53	21.28 ± 0.02	20.21 ± 0.01	19.61 ± 0.01	18.3	B
2	30.3615	-10.7597	$0.563^{+0.607}_{-0.521}$	4.17	23.37 ± 0.07	21.96 ± 0.05	21.17 ± 0.02	15.9	A
3	30.4522	-7.5357	$0.393^{+0.437}_{-0.335}$	4.51	22.38 ± 0.04	21.47 ± 0.03	21.02 ± 0.02	33.7	B
4	30.7655	-4.4937	$0.387^{+0.423}_{-0.353}$	3.90	21.56 ± 0.02	20.31 ± 0.01	19.73 ± 0.01	12.1	B
5	30.9987	-8.3652	$0.495^{+0.529}_{-0.459}$	4.48	21.48 ± 0.02	20.30 ± 0.01	19.76 ± 0.01	9.3	B
6	31.0361	-9.6104	$0.409^{+0.463}_{-0.363}$	3.83	22.00 ± 0.02	20.70 ± 0.01	20.03 ± 0.01	16.9	A
7	31.2852	-3.9099	$0.252^{+0.294}_{-0.227}$	5.22	20.56 ± 0.01	19.76 ± 0.01	19.31 ± 0.01	7.06	A
8	31.4770	-6.4598	$0.442^{+0.473}_{-0.411}$	5.32	20.98 ± 0.02	19.69 ± 0.01	19.17 ± 0.01	7.8	B
9	31.9736	-8.8432	$0.289^{+0.359}_{-0.243}$	5.30	20.55 ± 0.01	19.83 ± 0.01	19.47 ± 0.01	11.6	B
10	32.2221	-6.9186	$0.902^{+0.939}_{-0.866}$	6.40	22.28 ± 0.04	21.82 ± 0.05	20.91 ± 0.03	13.5	A
11	32.3970	-8.3013	$0.611^{+0.641}_{-0.580}$	4.23	21.85 ± 0.03	20.63 ± 0.01	19.81 ± 0.01	8.6	A
12	32.4703	-6.5295	$0.389^{+0.414}_{-0.351}$	3.90	20.00 ± 0.01	19.12 ± 0.00	18.65 ± 0.00	9.03	A
13	32.5096	-3.7956	$0.556^{+0.595}_{-0.515}$	7.29	21.60 ± 0.03	20.48 ± 0.02	19.86 ± 0.01	9.4	A
14	32.6591	-7.4773	$0.478^{+0.504}_{-0.453}$	3.05	22.93 ± 0.05	21.44 ± 0.02	20.64 ± 0.01	30.0	A
15	32.8441	-4.3681	$0.731^{+0.759}_{-0.703}$	4.36	23.13 ± 0.08	21.81 ± 0.03	20.49 ± 0.02	17.4	A
16	32.9734	-5.9950	$0.139^{+0.190}_{-0.050}$	5.98	19.29 ± 0.00	18.69 ± 0.00	18.31 ± 0.00	6.6	B
17	33.0833	-7.9352	$0.451^{+0.477}_{-0.428}$	7.58	21.06 ± 0.01	20.26 ± 0.01	19.64 ± 0.01	6.7	A
18	33.1342	-6.6479	$0.450^{+0.481}_{-0.421}$	6.13	20.94 ± 0.01	20.01 ± 0.01	19.63 ± 0.01	9.2	A
19	33.1958	-5.8338	$0.809^{+0.853}_{-0.768}$	5.96	21.76 ± 0.02	21.16 ± 0.03	20.36 ± 0.02	6.3	B
20	33.6128	-9.0673	$0.698^{+0.724}_{-0.670}$	4.08	22.44 ± 0.04	21.25 ± 0.02	20.17 ± 0.01	8.3	A
21	33.6250	-9.1754	$0.398^{+0.433}_{-0.366}$	5.64	21.16 ± 0.01	20.01 ± 0.01	19.59 ± 0.01	10.1	A
22	33.8107	-4.7156	$0.346^{+0.378}_{-0.313}$	5.55	20.40 ± 0.01	19.32 ± 0.01	18.83 ± 0.01	10.3	A
23	33.9600	-4.4247	$0.388^{+0.417}_{-0.359}$	5.23	20.32 ± 0.01	19.31 ± 0.01	18.88 ± 0.01	9.4	B
24	34.9904	-6.5704	$0.486^{+0.510}_{-0.464}$	3.54	22.72 ± 0.04	21.26 ± 0.02	20.43 ± 0.01	13.8	A
25	35.0485	-6.8143	$0.489^{+0.525}_{-0.454}$	5.72	20.85 ± 0.01	19.90 ± 0.01	19.45 ± 0.01	6.5	A
26	35.0763	-5.6397	$0.709^{+0.749}_{-0.676}$	5.34	22.29 ± 0.03	21.66 ± 0.04	21.09 ± 0.03	6.2	B
27	35.1759	-8.1834	$0.361^{+0.384}_{-0.337}$	4.90	20.51 ± 0.01	19.53 ± 0.01	19.18 ± 0.01	7.2	A
28	35.3647	-9.9535	$0.772^{+0.815}_{-0.732}$	4.32	23.06 ± 0.06	22.19 ± 0.05	21.13 ± 0.03	21.9	A
29	35.5374	-5.6453	$0.457^{+0.496}_{-0.420}$	6.31	21.06 ± 0.01	20.21 ± 0.01	19.93 ± 0.01	7.5	A
30	37.0163	-5.8651	$0.400^{+0.448}_{-0.356}$	2.66	22.78 ± 0.03	21.68 ± 0.03	21.27 ± 0.02	7.6	B
31	37.1982	-3.9803	$0.680^{+0.711}_{-0.651}$	9.24	21.66 ± 0.04	20.70 ± 0.03	19.93 ± 0.02	9.8	B
32	37.5014	-7.8604	$0.591^{+0.630}_{-0.549}$	3.85	22.96 ± 0.05	21.79 ± 0.03	21.01 ± 0.02	12.7	B
33	37.5045	-5.7003	$0.559^{+0.594}_{-0.525}$	4.96	21.31 ± 0.02	20.16 ± 0.01	19.54 ± 0.01	7.6	A
34	38.0929	-3.7355	$0.798^{+0.848}_{-0.762}$	9.60	22.03 ± 0.05	21.38 ± 0.05	20.41 ± 0.03	10.5	B
35	38.2284	-5.3160	$0.710^{+0.760}_{-0.665}$	4.57	23.10 ± 0.05	22.36 ± 0.06	21.73 ± 0.05	10.7	A
36	132.1016	-5.1126	$0.412^{+0.439}_{-0.388}$	7.33	21.02 ± 0.01	19.99 ± 0.01	19.50 ± 0.01	7.1	A
37	132.1377	-4.8329	$0.774^{+0.804}_{-0.745}$	2.18	22.99 ± 0.04	21.86 ± 0.03	20.65 ± 0.01	13.3	A
38	132.5373	-4.2216	$0.222^{+0.257}_{-0.186}$	4.96	19.66 ± 0.00	18.70 ± 0.00	18.25 ± 0.00	9.8	A
39	133.2203	-3.9328	$0.430^{+0.458}_{-0.401}$	8.14	20.49 ± 0.01	19.49 ± 0.01	19.12 ± 0.01	10.6	A
40	133.5310	-4.1230	$0.670^{+0.698}_{-0.641}$	8.29	22.18 ± 0.04	21.22 ± 0.04	20.44 ± 0.02	14.5	A
41	133.7787	-3.8646	$0.715^{+0.745}_{-0.687}$	8.10	21.60 ± 0.02	20.67 ± 0.03	19.85 ± 0.01	10.4	A
42	134.4040	-2.8884	$0.687^{+0.726}_{-0.660}$	5.44	22.05 ± 0.03	21.37 ± 0.02	20.76 ± 0.02	7.2	B
43	135.0560	-3.0676	$0.608^{+0.648}_{-0.566}$	5.33	22.53 ± 0.05	21.33 ± 0.04	20.54 ± 0.02	9.1	A
44	135.2780	-1.8642	$0.353^{+0.385}_{-0.322}$	6.13	20.47 ± 0.01	19.51 ± 0.01	19.11 ± 0.01	11.2	A
45	135.4850	-2.5134	$0.689^{+0.716}_{-0.663}$	5.91	22.16 ± 0.04	21.22 ± 0.02	20.49 ± 0.02	6.7	A
46	208.9030	57.0818	$0.392^{+0.420}_{-0.366}$	5.15	21.42 ± 0.02	20.26 ± 0.01	19.74 ± 0.01	6.4	A
47	208.9420	57.1261	$0.406^{+0.434}_{-0.383}$	6.76	20.32 ± 0.01	19.33 ± 0.01	18.92 ± 0.01	11.0	A
48	209.2140	54.2889	$0.574^{+0.616}_{-0.515}$	5.09	21.45 ± 0.02	20.64 ± 0.01	20.18 ± 0.01	5.4	A
49	209.3525	55.6741	$0.398^{+0.429}_{-0.374}$	7.07	20.29 ± 0.01	19.31 ± 0.01	18.93 ± 0.01	14.2	B
50	209.3780	53.4301	$0.370^{+0.399}_{-0.329}$	4.96	20.44 ± 0.01	19.53 ± 0.01	19.08 ± 0.01	8.2	A
51	209.6380	55.8449	$0.376^{+0.399}_{-0.352}$	4.92	20.02 ± 0.00	18.99 ± 0.00	18.55 ± 0.00	9.8	A
52	209.7398	57.0189	$0.303^{+0.343}_{-0.256}$	6.29	20.66 ± 0.01	19.44 ± 0.01	18.93 ± 0.01	14.1	B
53	209.7620	53.3673	$0.331^{+0.374}_{-0.277}$	4.86	21.10 ± 0.02	19.77 ± 0.01	19.21 ± 0.01	12.2	A
54	209.8280	57.4606	$0.396^{+0.432}_{-0.363}$	5.92	21.60 ± 0.02	20.38 ± 0.01	19.87 ± 0.01	11.7	A
55	209.8940	54.8880	$0.456^{+0.487}_{-0.424}$	4.40	20.61 ± 0.01	19.81 ± 0.01	19.45 ± 0.01	7.1	B
56	209.8970	56.7132	$0.307^{+0.339}_{-0.274}$	5.00	20.28 ± 0.01	19.31 ± 0.00	18.85 ± 0.01	7.6	B
57	209.9210	56.1383	$0.370^{+0.400}_{-0.340}$	8.58	20.52 ± 0.01	19.41 ± 0.01	18.92 ± 0.01	11.2	A
58	210.0069	56.9977	$0.377^{+0.398}_{-0.352}$	7.27	20.52 ± 0.01	19.58 ± 0.01	19.19 ± 0.01	9.7	B

Table 1. List of grade-*A* and grade-*B* new lens candidates in CFHTLS. The photometric redshifts z, the effective radius $R_{\rm eff}$ and the magnitudes are the ones provided by Coupon et al. (2009).

that are more frequently contained either within the equatorial or polar planes. Since the polar rings are blue and nearly perpendicular to the semi-major axis of their central hosts, they closely

ID	RA	DEC	z	$R_{\rm eff}$	g	r	i	$R_{\rm E}$	Quality
				pix	mag	mag	mag	pix	
59	210.3022	56.2394	$0.412^{+0.446}_{-0.382}$	4.81	20.93 ± 0.01	19.58 ± 0.01	18.99 ± 0.01	14.7	B
60	210.3220	57.3084	$0.382^{+0.412}_{-0.348}$	7.61	20.08 ± 0.01	19.47 ± 0.01	19.17 ± 0.01	9.1	A
61	210.3420	57.0673	$0.810^{+0.905}_{-0.757}$	2.73	22.92 ± 0.06	22.52 ± 0.05	21.98 ± 0.05	7.9	B
62	210.5270	53.4316	$0.564^{+0.601}_{-0.529}$	7.80	21.29 ± 0.03	20.06 ± 0.01	19.36 ± 0.01	8.9	A
63	210.5496	57.5600	$0.759^{+0.792}_{-0.727}$	9.35	21.89 ± 0.05	20.97 ± 0.03	20.11 ± 0.02	14.8	A
64	210.5840	51.7352	$0.214^{+0.250}_{-0.175}$	4.40	19.79 ± 0.00	18.92 ± 0.00	18.47 ± 0.00	9.4	A
65	211.4080	57.6165	$0.306^{+0.340}_{-0.271}$	6.51	20.33 ± 0.01	19.43 ± 0.01	19.03 ± 0.01	8.9	A
66	211.8142	57.1322	$0.322^{+0.353}_{-0.289}$	6.09	20.02 ± 0.01	18.94 ± 0.00	18.50 ± 0.00	11.6	A
67	211.8690	52.6938	$0.485^{+0.516}_{-0.448}$	6.44	21.18 ± 0.02	20.03 ± 0.01	19.56 ± 0.01	7.1	A
68	211.9780	56.2218	$0.387^{+0.412}_{-0.364}$	7.21	21.08 ± 0.01	19.99 ± 0.01	19.56 ± 0.01	8.9	A
69	212.0175	56.2446	$0.370^{+0.400}_{-0.339}$	5.01	21.05 ± 0.01	19.88 ± 0.01	19.36 ± 0.01	10.1	A
70	212.1570	52.3579	$0.855^{+0.899}_{-0.819}$	6.39	21.78 ± 0.03	21.05 ± 0.03	20.16 ± 0.02	7.7	A
71	212.2455	51.8158	$0.343^{+0.373}_{-0.315}$	7.97	21.02 ± 0.02	20.55 ± 0.02	20.50 ± 0.02	11.2	A
72	212.3657	53.5918	$0.421^{+0.455}_{-0.389}$	5.84	20.84 ± 0.01	19.66 ± 0.01	19.16 ± 0.01	13.1	B
73	212.6040	54.0908	$0.420^{+0.457}_{-0.383}$	5.63	20.84 ± 0.01	19.68 ± 0.01	19.25 ± 0.01	12.4	A
74	212.7290	54.9406	$0.469^{+0.510}_{-0.429}$	4.91	21.75 ± 0.02	20.53 ± 0.01	19.89 ± 0.01	9.7	B
75	212.8450	51.6687	$0.499^{+0.536}_{-0.455}$	4.70	21.66 ± 0.02	20.41 ± 0.01	19.80 ± 0.01	6.5	A
76	213.0320	52.9143	$0.507^{+0.560}_{-0.463}$	6.89	21.07 ± 0.02	20.28 ± 0.01	19.86 ± 0.02	8.9	A
77	213.1650	53.9570	$0.436^{+0.469}_{-0.403}$	7.82	20.64 ± 0.01	19.53 ± 0.01	19.05 ± 0.01	8.2	A
78	213.4510	51.7295	$0.350^{+0.384}_{-0.311}$	7.57	19.92 ± 0.01	19.01 ± 0.01	18.58 ± 0.01	13.6	A
79	213.5430	52.8470	$0.393^{+0.424}_{-0.366}$	6.62	20.86 ± 0.01	19.83 ± 0.01	19.40 ± 0.01	7.3	A
80	213.6000	57.6236	$0.529^{+0.559}_{-0.496}$	5.81	21.84 ± 0.03	20.69 ± 0.02	20.19 ± 0.01	6.4	A
81	213.9140	54.8451	$0.232^{+0.266}_{-0.202}$	6.64	18.79 ± 0.00	18.05 ± 0.00	17.65 ± 0.00	11.9	A
82	214.4110	56.3307	$0.590^{+0.619}_{-0.553}$	5.54	21.76 ± 0.02	20.76 ± 0.02	20.04 ± 0.01	8.3	B
83	214.5100	57.3730	$0.570^{+0.609}_{-0.535}$	6.41	21.15 ± 0.02	20.19 ± 0.01	19.74 ± 0.01	7.7	A
84	214.5255	54.2536	$0.738^{+0.775}_{-0.707}$	4.95	22.23 ± 0.03	21.22 ± 0.03	20.21 ± 0.01	18.3	A
85	214.9620	51.8585	$0.682^{+0.709}_{-0.658}$	3.83	22.01 ± 0.02	21.16 ± 0.02	20.45 ± 0.02	8.9	B
86	215.3410	56.2251	$0.546^{+0.583}_{-0.508}$	5.86	21.08 ± 0.01	20.23 ± 0.01	19.78 ± 0.01	7.4	A
87	215.6690	57.0355	$0.433^{+0.467}_{-0.401}$	4.90	20.54 ± 0.01	19.41 ± 0.01	18.91 ± 0.01	9.2	A
88	216.3770	56.4335	$0.508^{+0.538}_{-0.475}$	7.41	20.86 ± 0.01	19.62 ± 0.01	19.01 ± 0.01	11.1	A
89	216.5700	55.1213	$0.629^{+0.655}_{-0.602}$	5.90	21.73 ± 0.02	20.66 ± 0.02	19.80 ± 0.01	9.2	A
90	216.7250	56.1682	$0.240^{+0.268}_{-0.210}$	6.96	19.97 ± 0.01	19.27 ± 0.01	18.90 ± 0.01	13.7	B
91	217.0550	54.8198	$0.855^{+0.894}_{-0.814}$	4.50	23.40 ± 0.08	22.12 ± 0.04	20.97 ± 0.02	18.4	B
92	217.1570	55.4547	$0.651^{+0.679}_{-0.622}$	6.09	22.16 ± 0.03	21.09 ± 0.02	20.21 ± 0.02	8.4	B
93	217.4450	54.6213	$0.639^{+0.667}_{-0.609}$	6.02	21.55 ± 0.02	20.84 ± 0.02	20.28 ± 0.01	6.5	B
94	217.9957	55.7248	$0.465^{+0.507}_{-0.427}$	8.14	19.95 ± 0.01	19.04 ± 0.00	18.69 ± 0.01	9.9	A
95	218.4500	57.6522	$0.307^{+0.339}_{-0.274}$	6.68	19.74 ± 0.01	18.70 ± 0.00	18.26 ± 0.00	11.8	A
96	218.9394	55.9681	$0.734^{+0.758}_{-0.711}$	7.15	21.03 ± 0.01	20.25 ± 0.01	19.78 ± 0.01	11.4	B
97	218.9660	57.6901	$0.616^{+0.656}_{-0.563}$	6.94	21.96 ± 0.05	20.99 ± 0.03	20.26 ± 0.02	12.4	B
98	330.2529	2.2095	$0.250^{+0.285}_{-0.218}$	5.42	19.84 ± 0.01	18.94 ± 0.01	18.48 ± 0.01	11.3	A
99	330.6014	3.9024	$0.316^{+0.347}_{-0.284}$	5.65	20.17 ± 0.01	19.03 ± 0.01	18.56 ± 0.00	11.8	A
100	330.6080	2.1078	$1.008^{+1.062}_{-0.951}$	6.13	21.79 ± 0.03	21.39 ± 0.04	20.57 ± 0.03	7.2	B
101	331.3547	0.9742	$0.621^{+0.650}_{-0.588}$	5.34	22.00 ± 0.03	20.95 ± 0.02	20.26 ± 0.01	8.3	B
102	331.6466	2.2712	$0.334^{+0.375}_{-0.297}$	3.88	21.51 ± 0.02	20.06 ± 0.01	19.49 ± 0.01	21.1	B
103	331.8250	3.5431	$0.411^{+0.450}_{-0.380}$	6.03	21.45 ± 0.02	20.40 ± 0.02	20.00 ± 0.01	7.9	B
104	331.8586	1.4529	$0.373^{+0.396}_{-0.347}$	7.66	20.39 ± 0.01	19.48 ± 0.01	19.14 ± 0.01	7.7	A
105	332.0030	2.6561	$0.466^{+0.502}_{-0.426}$	4.09	21.76 ± 0.02	20.64 ± 0.02	20.15 ± 0.01	10.7	B
106	332.3005	3.7471	$0.270^{+0.298}_{-0.239}$	4.36	21.95 ± 0.02	21.19 ± 0.02	20.77 ± 0.02	14.8	A
107	332.3815	-0.2096	$0.472^{+0.509}_{-0.429}$	8.11	20.38 ± 0.01	19.40 ± 0.01	19.09 ± 0.01	8.4	B
108	334.0200	1.8810	$0.764^{+0.794}_{-0.735}$	7.28	21.75 ± 0.03	20.98 ± 0.03	20.14 ± 0.02	11.2	A
109	335.5896	-0.2775	$0.291^{+0.324}_{-0.257}$	5.69	20.14 ± 0.01	19.12 ± 0.01	18.62 ± 0.00	13.3	B

Table 2. List of grade-*A* and grade-*B* new lens candidates in CFHTLS. The photometric redshifts z, the effective radius $R_{\rm eff}$ and the magnitudes are the ones provided by Coupon et al. (2009).

resemble Einstein rings that are produced by gravitational lensing.

In our visual procedure, we attempt to classify an object as a ring galaxy if i) the ring structure has an ellipticity $\epsilon > 0.2$, or ii) the ring shows a surface brightness close to constant. Our criterion on the ellipticity comes from the fact that only very extreme, rare, and rather unphysical lens galaxies or systems with extreme external shear can create a strongly elongated Einstein ring. Very elliptical Einstein rings are therefore not expected. In fact, none are known in the current literature. On the contrary, gaseous rings around polar ring galaxies can be strongly elliptical, simply due to orientation effects. The second condition, i.e. constant surface brightness, comes from the fact that Einstein rings are never fully symmetric and that lensed sources have structures, i.e. a bulge, spiral arms, etc. Ring galaxies have more uniform light distributions across the gaseous ring.

Using the above criteria, the PCA-finder provides a list of 1 098 lens candidates that split, after visual classification, into:

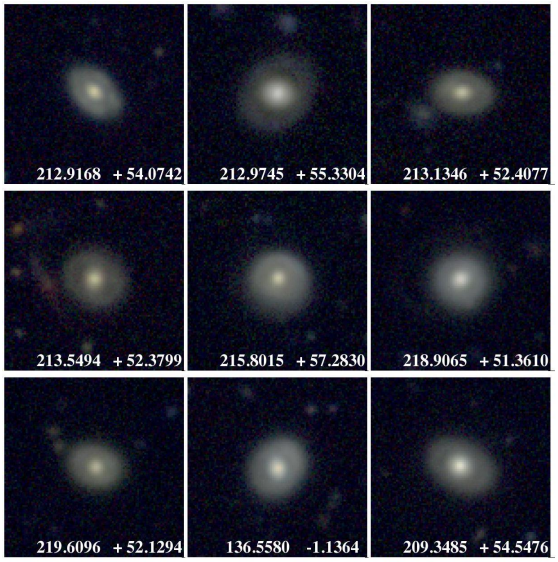

Fig. 5. Examples of objects producing false positives in our lens search and that we classify as ring-like galaxies or polar ring galaxies (see text). Among 1 098 lens candidates, we identify 274 of these ring-like galaxies.

- 70 grade-*A* candidates (Tables 1 & 2),
- 39 grade-*B* candidates (Tables 1 & 2),
- 183 grade-*C* candidates (Table A.2 of the Appendix),
- 274 ring-galaxies or polar-ring galaxies (Table A.1 of the Appendix).

All our newly discovered grade-*A* and grade-*B* lens candidates are shown in Figs. A.1- A.5 of the Appendix [4]. Despite the visual classification, all above candidates would need spectroscopic and/or high-resolution photometric follow-up, which is beyond the scope of this paper. In the following we compare the properties of our sample of 109 (new) grade-*A* and grade-*B* lenses with other lens samples found in the CFHTLS data.

4.2. Comparison with previous searches

The CFHTLS data comprise all desirable survey properties for a lens search. They have been extensively explored in the past with a range of automated lens-finders, leading to very different lens samples. This clearly illustrates that no single technique can detect all the types of lenses at once and that current lens-finders are complementary. Some favour specific types of lensing object, such as spiral or elliptical galaxies, and others may select only massive lenses, e.g. by pre-selecting lenses as galaxy groups or clusters. Other favour a given source geometry, e.g. point sources (AGNs, quasars) or extended arcs and rings. Here, we give a brief summary of previously published CFHTLS lens samples and we attempt to understand why the PCA-finder method finds some but not all lenses from the published samples.

A lens sample that is significantly different from the one in the present paper is provided by Elyiv et al. (2013) and Sygnet et al. (2010). On the one hand Elyiv et al. (2013) searched for gravitational lens candidates among the optical counterparts of X-ray-selected QSOs/AGNs. The authors visually inspect a sample of 5 500 optical counterparts of X-ray point-like sources identified in the XMM-LSS imaging of the CFHTLS W1 field.

[4] FITS images of our lens candidates are also available at https://github.com/herjy/PiCARD

ID	RA	DEC	i	$z_{\rm phot}$
ArcFinder by More et al. (2016)				
1	30.6619	-6.5823	19.54	0.37
2	30.8351	-7.5808	19.45	0.59
3	33.8459	-7.6065	20.89	1.05
4	35.2351	-7.7199	20.51	0.71
5	35.8142	-6.4851	19.21	0.55
6	36.5298	-4.4573	17.97	0.17
7	132.0986	-4.1209	18.85	0.51
8	134.4546	-1.2169	18.26	0.29
9	210.4371	53.0360	19.61	0.56
10	214.8007	53.4365	19.11	0.69
11	214.8219	51.2913	18.72	0.47
12	217.9695	57.4769	20.19	0.83
13	217.1451	52.2185	19.94	0.52
14	217.5027	55.7799	19.12	0.55
15	330.8709	2.0886	19.37	0.38
16	331.2788	1.7844	19.15	0.46
17	333.2789	-0.5103	18.81	0.69
18	333.5784	1.1761	18.84	0.74
ArcFinder by Maturi et al. (2014)				
1	33.5688	-5.0548	21.00	0.37
2	34.9856	-6.0341	20.50	0.42
3	36.4030	-4.2549	22.10	0.56
4	37.2865	-5.3320	22.40	0.37
5	209.2597	52.5104	23.00	0.38
6	209.6937	52.3495	23.40	0.35
7	210.0883	52.2626	21.20	0.76
8	335.5734	0.2007	21.70	0.51

Table 3. Strong lenses found using the two different ArcFinders (see text), and that we also find in the present work with the PCA-finder.

They find three good gravitational lens candidates. Sygnet et al. (2010), on other hand, look for lensing events produced only by massive edge-on disk galaxies. In their search, they preselect only highly elongated objects with $0.7 > \epsilon > 0.9$. Their final sample, which also involves a visual inspection, has 16 lens candidates. The PCA-finder neither looks for point-like multiple images nor for elongated lenses, thus we do not expect our search to recover any of those published lenses.

To the best of our knowledge, there are four lens searches similar to ours in CFHTLS (Gavazzi et al. 2014; More et al. 2012; Maturi et al. 2014; More et al. 2016). More et al. (2012) built a sample of lenses using ArcFinder with a setting such that only systems with arc radii larger than 2″ are kept in the sample. Their lens sample with large Einstein radii therefore predominantly selects group and cluster-scale lenses. ArcFinder measures the second order moments of the flux distribution in pixels within small regions of the sky to estimate the direction and extent of local elongation of features. Then, a set of thresholds on feature properties such as the area, length, width, curvature and surface brightness were used to select arc-like candidates. The search was carried out in the g band which is the most efficient wavelength to find typical lensed features. The ArcFinder final sample consists of 55 promising lenses out of a total of 127 lens candidates, which are selected from both CFHTLS *Wide* and *Deep* fields. The PCA-finder recovers 16 out of these 127 candidates. This low fraction of recovered systems is somewhat expected since the majority of the systems found by ArcFinder consist of multiple lensing galaxies, which are not recoverable by our method. PCA-finder detects arcs and rings that are centred on single lensing galaxies, any of the lensing features around

RingFinder by Gavazzi et al. (2014)				
ID	RA	DEC	i	$z_{\rm phot}$
1	31.0368	-6.2019	19.92	0.440
2	31.3527	-9.5065	19.46	0.697
3	32.7569	-8.9320	20.67	0.562
4	33.2527	-8.7196	19.26	0.471
5	33.9505	-3.7979	19.7	0.577
6	34.6119	-7.2910	20.02	0.474
7	35.2352	-7.7199	20.48	0.688
8	35.6735	-5.6477	19.50	0.502
9	36.4030	-4.2549	19.60	0.631
10	36.5152	-9.7643	18.30	0.229
11	36.6384	-3.8179	20.08	0.652
12	36.7455	-8.0105	19.06	0.450
13	37.1431	-8.7207	19.08	0.493
14	37.9618	-4.2917	19.69	0.838
15	38.6843	-6.8091	20.32	0.728
16	133.3229	-2.0543	20.51	0.706
17	133.7865	-3.1020	20.64	0.613
18	134.3794	-1.0678	18.72	0.660
19	136.5196	-3.9364	19.51	0.776
20	210.0897	51.5229	19.82	0.523
21	210.0947	54.9680	20.01	0.703
22	210.1774	56.0118	19.26	0.568
23	210.6061	56.6629	20.32	0.662
24	210.9173	56.7688	19.54	0.689
25	211.0588	51.7374	19.69	0.645
26	211.1062	52.0850	18.82	0.522
27	211.3248	54.5971	20.48	0.726
28	211.8857	54.5689	19.03	0.411
29	212.2298	52.7479	19.98	0.492
30	213.9302	52.4597	19.17	0.445
31	214.8219	51.2913	18.72	0.468
32	215.0140	52.5271	20.99	0.510
33	215.1154	54.1452	18.54	0.421
34	215.1325	52.9728	18.87	0.461
35	215.1830	54.8169	19.97	0.727
36	215.8413	57.3786	19.11	0.611
37	216.0988	52.5648	18.31	0.277
38	216.1354	55.0055	19.39	0.451
39	217.8799	57.1606	18.71	0.454
40	218.5875	54.6375	20.29	0.728
41	219.1557	54.9436	19.05	0.360
42	219.7768	54.6502	19.33	0.378
43	330.8709	2.0886	19.37	0.380
44	331.2789	1.7845	19.15	0.460
45	332.1596	3.0189	18.51	0.302
46	333.3725	0.4932	18.91	0.483
47	333.4006	0.1964	20.34	0.623
48	333.4959	0.9046	18.27	0.370
49	335.4535	1.2618	18.35	0.346
50	335.5735	0.2008	19.13	0.421

Table 4. Strong lenses discovered with the RingFinder and also found by the PCA-finder.

groups or cluster of galaxies are lost. Table 3 lists the lenses found both by the PCA-finder and with ArcFinder.

Maturi et al. (2014) devised an automated lens-finder based on the colour statistics of arcs using a model for the spectral energy distribution (SED) of high redshift galaxies, the lensing optical depth, and the data depth. They therefore find lensed sources not only based on their morphology, but also from their colour, selecting the colours corresponding to sources providing the largest possible lensing cross-section. Using this procedure, which combines the ArcFinder created by Seidel & Bartelmann (2007), with a fine-tuned colour selection, they significantly increased the CFHTLS sample of gravitational lenses. They apply their method to the CFHTLS Archive Research Survey (CARS; Erben et al. 2009) data, which covers 37 square degrees, to verify its efficiency and to detect new gravitational arcs. Table 3 lists the lenses found both by the PCA-finder and by Maturi et al. (2014).

Space Warps by More et al. (2016)				
ID	RA	DEC	i	$z_{\rm phot}$
1	31.6759	-9.8669	20.8	0.2
2	32.1339	-4.5542	21.0	1.0
3	33.1051	-8.8697	19.5	0.8
4	135.5794	-5.6566	0.0	0.0
5	211.5958	52.1617	20.3	0.7
6	216.5869	56.2323	19.5	0.5
7	216.7205	56.0016	0.0	0.0
8	217.3907	56.4277	19.0	0.5
9	217.7351	57.4084	19.3	0.7
10	219.2150	53.1183	19.2	0.6

Table 5. Galaxy-scale lensed systems found in the context of the Space Warps project that are also detected by our PCA-finder.

Gavazzi et al. (2014) use their RingFinder tool to search for galaxies lensed by massive foreground early-type galaxies. The principle of RingFinder is similar to ours: they select all early-type galaxies from CFHTLS and then subtract them from the images to find lensing features. There are two main differences between our work and Gavazzi et al. (2014): the way the lenses are subtracted from the images and the way the residual images are analysed. To remove the central galaxy, Gavazzi et al. (2014) subtracts the PSF-matched i-band images from the g-band images. On the residual image, they looked for excess flux in the g-band to search for compact lensing signal, i.e. multiply-imaged point sources, rings and arcs. In total 2 524 objects passed their automatic selection procedure. These are visually inspected, leading to a total of 330 lens candidates, out of which 42 were ranked as good quality lenses and 288 were in their medium-quality category. In addition to the main sample of Gavazzi et al. (2014), another 71 candidates were reported to have been detected by earlier versions of the RingFinder. From the main sample of RingFinder, during their follow-up campaign, they confirmed 33 lenses. Out of the 330 medium and high quality candidates found with RingFinder, 50 are also found by our PCA-finder (Table 4).

Finally, the most recent CFHTLS lens search is known as Space Warps by More et al. (2016) and is fully based on a visual detection and classification of lensing systems by humans, namely "citizen" that volunteer to inspect the CFHTLS colour images. They report the discovery of 29 promising new lens candidates out of a total 59 candidates, based on about 11 million classifications performed by motivated citizen scientists. The goal of the blind lens search was to identify lens candidates missed by automated searches. This type of massive visual search enables us to catch a larger diversity in lens and source properties than automated searches (see also Pawase et al. 2014, for an example of a visual search in the HST database). Our PCA-finder recovers ten out of the 29 best candidates found in Space Warps. These are listed in Table 5.

Our PCA-finder cannot be expected to recover all the RingFinder and Space Warps lenses, owing to the different levels of incompleteness of the different searches but also because of the pre-selection of galaxies in the PCA-finder search. We target early-type galaxies as potential lenses and we apply a cut in size

for the lens galaxy (4-9 pixels). At least part of the lens candidates from the previous searches do not meet this size cut. We also note that the PCA-finder is not optimized to find multiply-imaged point sources, which are very well spotted visually in Space Warps and with RingFinder.

Finding gravitational lenses is a complex task, thus no single lens finding method is perfect, each method has advantages over the other. It may be the case that a single method may never be the best method for optimising completeness and purity. As a consequence, it is not surprising that in spite of the many previous extensive lens searches in CFHTLS, we still manage to find new, interesting candidates. The PCA-finder, despite being very close conceptually to the RingFinder, has two major advantages. First, it is applied efficiently on single-band data. We therefore apply it independently to all the bands. In this way the search is not restricted to a limited range of source colours. Second, the resulting lens subtraction leaves very few artefacts, hence allowing us to spot fainter lensed features closer to the lens centre.

We note that the 109 good lens candidates listed in Tables 1 & 2 are completely new. We also list 183 new objects in Table A.2 of the Appendix that we rank as possible lenses, but that certainly require follow-up with either deeper imaging or spectroscopy or both.

4.3. Sample properties

We now compare various properties of our lens candidates with previous samples from CFHTLS. We emphasise that these comparisons use lens candidates that are not yet confirmed and that our results are therefore only indicative.

We use the CFHTLS photometric catalogues from Coupon et al. (2009) and generated with the Le Phare software (Ilbert et al. 2006). The accuracy of the photometric redshifts of galaxies for the *Wide* survey with magnitudes $i < 21.5$ is $\sigma(\Delta z/(1+z)) = 0.032$. Figure 6 shows the distributions in apparent magnitude, Einstein radii and redshift for our PCA-finder sample of 70 grade-*A* plus 39 grade-*B* new gravitational lens candidates. These are shown together with the same distributions for Space Warps (More et al. 2016), for the ArcFinder (More et al. 2012), and for the RingFinder (Gavazzi et al. 2014). We find that the median of the lens redshift distribution for the PCA sample is $z_{\rm PCA} = 0.48 \pm 0.17$ and it is lower than redshift for all the other known lenses, which is $z_{\rm arcs} = 0.52 \pm 0.20$ (including giant arcs which systematically have larger redshifts). The median of *i*-band magnitude of our sample is $m_i = 19.63$, which turns into a median absolute magnitude of our sample $M_g = -21.90 \pm 0.745$. These magnitudes are K-corrected following Coupon et al. (2009).

The Einstein radii displayed in Fig. 6 are estimated from the position of the multiply-lensed images. R_E is taken to be half the averaged values of the angular separation between images. The distribution of image separations can be used to probe the average density profile of the lens population (Oguri et al. 2006; More et al. 2012). We find that the average Einstein radius for our new lenses is $R_E = 1.9 \pm 0.8''$ which is, as expected, smaller than for the ArcFinder candidates, which have $R_E = 4.0''$. This is also lower than for Space Wraps which have $R_E = 1.9''$. For comparison the SLACS lenses have $R_E = 2.2''$ and the RingFinder lenses is $R_E = 1.4''$ (see Sonnenfeld et al. 2013).

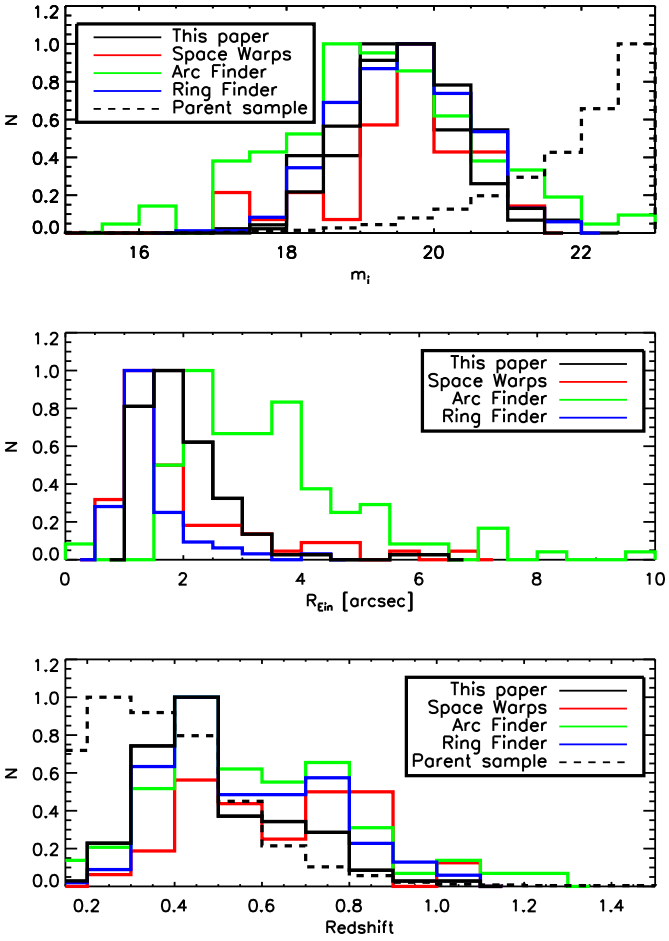

Fig. 6. *i*-band magnitude, Einstein radius, and redshift distributions of our lens candidates with *A* and *B* grades (black line). These are compared with the same distributions for other lens samples found in CFHTLS *Wide*: the one from the Space Warps program (red line; More et al. 2016), from the ArcFinder (green line; More et al. 2012) and from the RingFinder (blue line; Gavazzi et al. 2014). When applicable, we also show the distribution for the parent sample, i.e. our preselection of potential lens galaxies.

5. Simulations and completeness

An evaluation of the completeness of our sample can be done in two ways, using realistic image simulations or using a sample of already known lenses. The latter approach has been attempted in the previous section, but has a clear limitation: the reference sample of known lenses has its own completeness and purity. Moreover, different lens-finders are not necessarily optimised to find the same lens types and the parent samples (i.e. after the pre-selection) are not the same. As was shown in the previous section, one lens-finder can be very efficient at finding objects with low lens/source luminosity contrast, another one may be specialised in finding large arc-like structures and others may find better lensed point sources. For all these reasons, we choose to use simulated images for our completeness estimation.

In this section we evaluate the performances of our method using simulated images of Einstein rings, as they would be seen with the CFHT. We have made an attempt to generate lenses that are as realistic as possible within the requirements of the

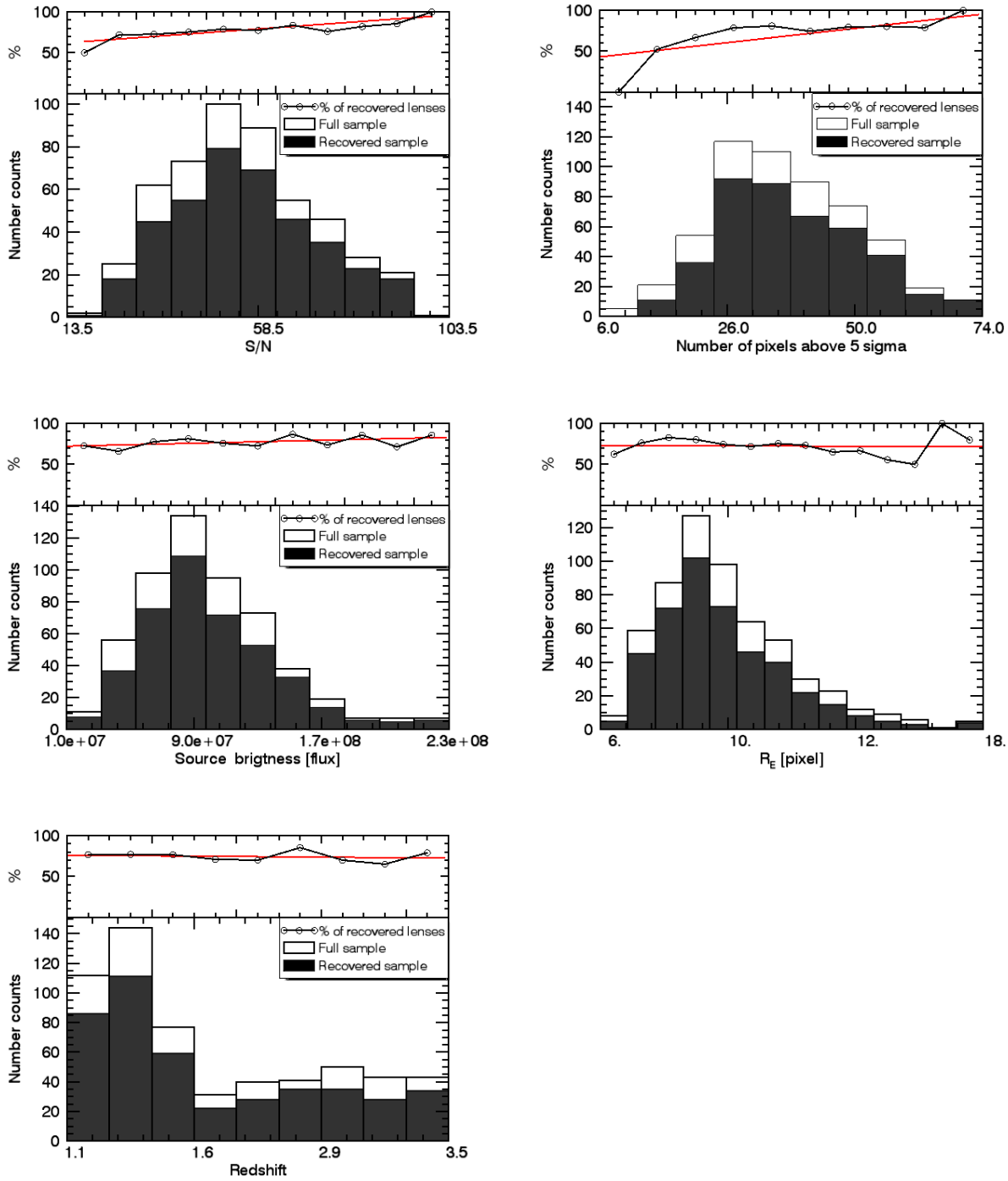

Fig. 7. Properties of the lensed systems for the simulated sample. Each plot in the lower panels shows the distributions of selected parameters of the full sample of simulated systems and for the simulated objects we identify as lenses (true positives). The top panels give the ratio of the two, i.e. the completeness per bin of the selected parameter. The red line is a linear regression to guide the eye.

PCA lens-finder. In the following, we also describe some of the properties of our simulated sample.

5.1. The lens and source simulation

The image simulations are provided by the Bologna Lens Factory (BLF). The BLF setup was chosen to match the properties of gravitational lenses expected in the CFHTLS wide fields by adding fake lensed objects to real images.

The lensing simulations were done as follows. A dark matter halo catalogue within a light cone extending out to $z = 4$ is taken from the Millennium Run Observatory (Overzier et al. 2013). This contains all the halos found within the Millennium cosmological simulation that were more massive than 10^{10} $M_{\odot}$, which

should include the hosts of all the observable strong lenses. The light cone covers 1.6 square degrees of sky. Each halo is represented within the lensing code by a Navarro, Frenk & White (NFW) halo plus a singular isothermal ellipsoid (SIE) in its centre to represent the baryonic component. The mass of the baryonic component is determined using the halo mass vs. stellar mass relation of Moster et al. (2010) and the velocity dispersion is set by the Tully-Fisher relation (Bell & de Jong 2001). Once the light cone is assembled, all the caustics in this light cone with Einstein radii $R_E > 0\farcs05$ are located, for a series of six source planes running from $z = 1$ to $z = 3.5$, using the GLAMER lensing code (Metcalf & Petkova 2014; Petkova et al. 2014). GLAMER shoots rays through the light cone and identifies regions of the source plane that will be strongly lensed. The code then adaptively shoots rays in these areas at higher and higher resolution to resolve the critical curves and caustic curves of each prospective lens.

The simulated image of a lensed source is then added to a real image of a galaxy that is randomly taken from the preselected CFTHLS data. This step was unavoidable, bearing in mind that the PCA lens extraction is solely based on the self-similarity of the foreground galaxies. Since the simulations need to be as close to real CFHTLS data as possible, we thus draw galaxies from the preselected targets in size, magnitude, colour, etc (see Sect. 2.2). Galaxies selected for the simulations in such manner, contain all the relevant limits that we face in real data. This gives us several advantages: 1. the simulation naturally includes the noise properties of the original data, 2. the level of complexity in galaxy shapes is well representative of the real data, far beyond the reach of analytical galaxies models, 3. the simulation includes blending effects with companion galaxies. Even though this approach gives us a reliable way to estimate the completeness of our sample, it does not allow us to evaluate its purity. This requires a priori knowledge of which galaxies are and which are not acting as lenses. Since the galaxies are drawn randomly from the real data, they can potentially contain lensed features that would affect the results. While a visual inspection would probably solve this problem, it could however bias the completeness.

We note that the distribution of lens properties should be generally reproduced in the simulations, but that it is not necessary to reproduce the statistics of the lenses to high precision for our purposes. In the next section, we characterise the lens-detection efficiency in terms of various parameters such as S/N, Einstein radius, etc. It is necessary that the simulations fully cover the range of these parameters, but not that they reproduce the predicted distribution of parameters precisely. These simulations meet this requirement.

5.2. Completeness of the new lens sample

Our simulations include 600 systems, which match well the properties of the galaxies we preselected in CFHTLS (Sect. 2.2), as well as the noise properties of the images. We run the PCA lens-finder in the exact same way as we do on the real data, excluding the last step of a visual inspection. Our results are summarised in Fig. 7, where we compare the distribution of some of the most important observational parameters for the full population of the simulated lenses and for the population of simulated systems, actually identified as such by the PCA lens-finder. The ratio between the two histograms in Fig. 7 gives the completeness.

In our analysis, we estimate the completeness as a function of the total S/N in the (lensed) source, the number of pixels of the source above the noise level (5σ), the source surface brightness, R_E (taken as half the averaged values of the angular separation between images) and the source redshift. We note that the calculation of the source S/N includes a noise contribution from the lensing galaxy, which can significantly impact the detection when the source and the lens overlap. Using our lens simulations we find that:

- Not surprisingly the completeness of the sample improves with increasing S/N, reaching at least 80% as soon as $S/N > 50$. Even for the lowest source S/N in the sample, the completeness is still above 50% and this number increases to 70% when $S/N > 20$. Of course, within a given S/N bin the sample spans a large range of Einstein ring size and source/lens luminosity contrast, but overall the completeness achieved by the PCA lens-finder is very high.
- The completeness depends strongly on the number of pixels above a given luminosity threshold of the lensed source. This affects the angular size of the lensed image and therefore also our ability to determine its shape (ring, full, or partial arc). Of course the more spatial resolution elements in a lensed source, the better it can be classified.
- The completeness has slightly weaker dependence on source surface brightness than on S/N of the lensed source. This shows that we fail to detect some lenses with arcs and rings that fall into the glare of the lensing galaxy. This also shows that central lensing galaxy removal with PCA method is not perfect and has an impact on the lens search.
- Importantly, there is little or no dependence of the completeness with respect to R_E or to the source redshift. This suggests that the PCA lens-finder is capable of providing unbiased samples of systems spanning a broad range of masses and redshifts, which is desirable for galaxy formation and evolution studies based on strong gravitational lensing.

6. Summary and conclusions

We have implemented a novel method, PCA-finder, for the automated detection of galaxy-scale strong gravitational lensing to a heavily explored survey, namely, the 155 square degree of imaging data of the CFHTLS *Wide*. With the PCA lens-finder we discover 109 (70 grade *A* and 39 grade *B*) brand new gravitational lens candidates. The discovery of such a large number of new lens candidates missed by other searches proves PCA-finder to be a powerful tool in discovering lenses.

The search was carried out in four steps. In Step 1, we create a uniform data cube consisting of small image stamps centred on preselected early-type galaxies. In Step 2, we subtract central galaxies from the image stamps. In Step 3, we analyse residual images created in Step 2 to look for lensing features with the `DBSCAN` method. In Step 4, a sample of 1 098 candidates are selected from this automated procedure. Finally, Step 5 is a visual inspection of the lens candidates by five authors of this paper (D.P., J-P.K., R.J., F.C., P.D.). Following this last step, all candidates are allocated *A*, *B*, or *C* grades.

In this paper, we present the new PCA-finder lenses and compare it with the previously known samples from the CFHTLS, namely, Space Wraps, RingFinder and ArcFinder. Our main results can be summarised as follows:

- PCA-finder works well as a discovery engine for gravitational lenses.
- We present a sample of 70 grade-*A* and 39 grade-*B* new gravitational lens candidates, and additional 183 grade-*C* worth

noticing, but with no strong evidence for lensing. We rediscover 86 lens candidates from various samples published in the literature.
– The PCA-finder selects lens systems whose statistical properties are well comparable with the RingFinder and ArcFinder samples, including the range of lens redshifts, magnitudes, and image separation.
– We also find 274 potential ring galaxies or polar ring galaxies.
– We use a sample of simulated lenses tailored to the CFHTLS *Wide* data to verify the completeness of our automated method.

The discovery of many new lens candidates through the first PCA-finder lens search illustrates the strength of the method, since we find lens candidates that other algorithms missed. Upcoming and planned wide field imaging surveys such as the DES, HSC, KIDS, Euclid and the LSST will produce a great amount of data. Reliable automated algorithms together with citizen blind search will be necessary to find lenses in these very large surveys. As shown in this paper, one approach for finding lenses from the entire survey data may not be sufficiently complete and pure. Thus, combining robotic methods for preselection with the citizen science approach for visual screening might be a good strategy for finding lenses in these large imaging surveys. For samples that are sufficiently cleaned by the automated part of the pipeline, the human time spent on the final classification remains acceptable.

Acknowledgements. This research is supported by the Swiss National Science Foundation (SNSF). B. Metcalf's research is funded under the European Seventh Framework Programme, Ideas, Grant no. 259349 (GLENCO).

References

Auger, M. W., Treu, T., Bolton, A. S., et al. 2009, ApJ, 705, 1099
Auger, M. W., Treu, T., Bolton, A. S., et al. 2010, ApJ, 724, 511
Bell, E. F. & de Jong, R. S. 2001, ApJ, 550, 212
Belokurov, V., Evans, N. W., Moiseev, A., et al. 2007, ApJ, 671, L9
Bertin, E. & Arnouts, S. 1996, A&AS, 117, 393
Blackburne, J. A., Wisotzki, L., & Schechter, P. L. 2008, AJ, 135, 374
Bolton, A. S., Brownstein, J. R., Kochanek, C. S., et al. 2012, ApJ, 757, 82
Bolton, A. S., Burles, S., Koopmans, L. V. E., et al. 2008, ApJ, 682, 964
Bolton, A. S., Burles, S., Koopmans, L. V. E., Treu, T., & Moustakas, L. A. 2006, ApJ, 638, 703
Brault, F. & Gavazzi, R. 2015, A&A, 577, A85
Browne, I. W. A., Wilkinson, P. N., Jackson, N. J. F., et al. 2003, MNRAS, 341, 13
Brownstein, J. R., Bolton, A. S., Schlegel, D. J., et al. 2012, ApJ, 744, 41
Bussmann, R. S., Pérez-Fournon, I., Amber, S., et al. 2013, ApJ, 779, 25
Cabanac, R. A., Alard, C., Dantel-Fort, M., et al. 2007, A&A, 461, 813
Cabanac, R. A., Valls-Gabaud, D., & Lidman, C. 2008, MNRAS, 386, 2065
Cao, S., Biesiada, M., Gavazzi, R., Piórkowska, A., & Zhu, Z.-H. 2015, ApJ, 806, 185
Collett, T. E. 2015, ApJ, 811, 20
Conley, A., Cooray, A., Vieira, J. D., et al. 2011, ApJ, 732, L35
Coupon, J., Ilbert, O., Kilbinger, M., et al. 2009, A&A, 500, 981
Courbin, F., Chantry, V., Revaz, Y., et al. 2011, A&A, 536, A53
Cuillandre, J.-C. J., Withington, K., Hudelot, P., et al. 2012, in Society of Photo-Optical Instrumentation Engineers (SPIE) Conference Series, Vol. 8448, Society of Photo-Optical Instrumentation Engineers (SPIE) Conference Series, 0
Dalal, N. & Kochanek, C. S. 2002, ApJ, 572, 25
Easter, M., Kriegel, H., Sander, J., & Xu, X. 1996, In Proceedings of the 2nd International Conference on Knowledge Discovery and Data Mining
Einstein, A. 1916, Annalen der Physik, 356, 639
Elyiv, A., Melnyk, O., Finet, F., et al. 2013, MNRAS, 434, 3305
Erben, T., Hildebrandt, H., Lerchster, M., et al. 2009, A&A, 493, 1197
Fassnacht, C. D., Moustakas, L. A., Casertano, S., et al. 2004, ApJ, 600, L155
Faure, C., Kneib, J.-P., Covone, G., et al. 2008, ApJS, 176, 19
Gavazzi, G., Fumagalli, M., Cucciati, O., & Boselli, A. 2010, A&A, 517, A73
Gavazzi, R., Cooray, A., Conley, A., et al. 2011, ApJ, 738, 125
Gavazzi, R., Marshall, P. J., Treu, T., & Sonnenfeld, A. 2014, ApJ, 785, 144
Gavazzi, R., Treu, T., Koopmans, L. V. E., et al. 2008, ApJ, 677, 1046
Gavazzi, R., Treu, T., Rhodes, J. D., et al. 2007, ApJ, 667, 176
González-Nuevo, J., Lapi, A., Fleuren, S., et al. 2012, ApJ, 749, 65
Gregg, M. D., Becker, R. H., Brotherton, M. S., et al. 2000, ApJ, 544, 142
Hezaveh, Y. D., Marrone, D. P., Fassnacht, C. D., et al. 2013, ApJ, 767, 132
Ilbert, O., Arnouts, S., McCracken, H. J., et al. 2006, A&A, 457, 841
Inada, N., Becker, R. H., Burles, S., et al. 2003, AJ, 126, 666
Inada, N., Oguri, M., Becker, R. H., et al. 2007, AJ, 133, 206
Inada, N., Oguri, M., Shin, M.-S., et al. 2012, AJ, 143, 119
Jiang, G. & Kochanek, C. S. 2007, ApJ, 671, 1568
Jolliffe, I. T. 1986, Principal component analysis
Joseph, R., Courbin, F., Metcalf, R. B., et al. 2014, A&A, 566, A63
Koopmans, L. V. E., Treu, T., Bolton, A. S., Burles, S., & Moustakas, L. A. 2006, ApJ, 649, 599
Magain, P., Surdej, J., Swings, J.-P., Borgeest, U., & Kayser, R. 1988, Nature, 334, 325
Marshall, P. J., Hogg, D. W., Moustakas, L. A., et al. 2009, ApJ, 694, 924
Maturi, M., Mizera, S., & Seidel, G. 2014, A&A, 567, A111
Metcalf, R. B. & Madau, P. 2001, ApJ, 563, 9
Metcalf, R. B. & Petkova, M. 2014, MNRAS, 445, 1942
More, A., Cabanac, R., More, S., et al. 2012, ApJ, 749, 38
More, A., Verma, A., Marshall, P. J., et al. 2016, MNRAS, 455, 1191
Moster, B. P., Somerville, R. S., Maulbetsch, C., et al. 2010, ApJ, 710, 903
Moustakas, L. A., Marshall, P., Newman, J. A., et al. 2007, ApJ, 660, L31
Myers, S. T., Jackson, N. J., Browne, I. W. A., et al. 2003, MNRAS, 341, 1
Negrello, M., Hopwood, R., De Zotti, G., et al. 2010, Science, 330, 800
Oguri, M., Inada, N., Clocchiatti, A., et al. 2008, AJ, 135, 520
Oguri, M., Inada, N., Pindor, B., et al. 2006, AJ, 132, 999
Oguri, M., Rusu, C. E., & Falco, E. E. 2014, MNRAS, 439, 2494
Oke, J. B. & Gunn, J. E. 1983, ApJ, 266, 713
Overzier, R., Lemson, G., Angulo, R. E., et al. 2013, MNRAS, 428, 778
Pawase, R. S., Courbin, F., Faure, C., Kokotanekova, R., & Meylan, G. 2014, MNRAS, 439, 3392
Peng, C. Y., Ho, L. C., Impey, C. D., & Rix, H.-W. 2010, AJ, 139, 2097
Petkova, M., Metcalf, R. B., & Giocoli, C. 2014, MNRAS, 445, 1954
Rathna Kumar, S., Tewes, M., Stalin, C. S., et al. 2013, A&A, 557, A44
Ratnatunga, K. U., Griffiths, R. E., & Ostrander, E. J. 1999, AJ, 117, 2010
Refsdal, S. 1964, MNRAS, 128, 307
Rusin, D. & Kochanek, C. S. 2005, ApJ, 623, 666
Rusin, D., Kochanek, C. S., Falco, E. E., et al. 2003, ApJ, 587, 143
Seidel, G. & Bartelmann, M. 2007, A&A, 472, 341
Sonnenfeld, A., Treu, T., Gavazzi, R., et al. 2012, ApJ, 752, 163
Sonnenfeld, A., Treu, T., Gavazzi, R., et al. 2013, ApJ, 777, 98
Surdej, J., Magain, P., Swings, J.-P., et al. 1987, Nature, 329, 695
Suyu, S. H. 2012, MNRAS, 426, 868
Suyu, S. H., Auger, M. W., Hilbert, S., et al. 2013, ApJ, 766, 70
Suyu, S. H., Marshall, P. J., Auger, M. W., et al. 2010, ApJ, 711, 201
Suyu, S. H., Treu, T., Hilbert, S., et al. 2014, ApJ, 788, L35
Sygnet, J. F., Tu, H., Fort, B., & Gavazzi, R. 2010, A&A, 517, A25
Tewes, M., Courbin, F., Meylan, G., et al. 2013, A&A, 556, A22
Tramacere, A. & Vecchio, C. 2013, Astronomy and Astrophysics, 549, A138
Treu, T., Auger, M. W., Koopmans, L. V. E., et al. 2010, ApJ, 709, 1195
Treu, T., Koopmans, L. V., Bolton, A. S., Burles, S., & Moustakas, L. A. 2006, ApJ, 640, 662
Treu, T. & Koopmans, L. V. E. 2004, ApJ, 611, 739
Treu, T., Stiavelli, M., Casertano, S., Møller, P., & Bertin, G. 2002, ApJ, 564, L13
Vegetti, S., Lagattuta, D. J., McKean, J. P., et al. 2012, Nature, 481, 341
Vuissoz, C., Courbin, F., Sluse, D., et al. 2008, A&A, 488, 481
Wardlow, J. L., Cooray, A., De Bernardis, F., et al. 2013, ApJ, 762, 59
Willis, J. P., Hewett, P. C., & Warren, S. J. 2005, MNRAS, 363, 1369
Willis, J. P., Hewett, P. C., Warren, S. J., Dye, S., & Maddox, N. 2006, MNRAS, 369, 1521
Winn, J. N., Hewitt, J. N., Patnaik, A. R., et al. 2001, AJ, 121, 1223
Winn, J. N., Hewitt, J. N., Schechter, P. L., et al. 2000, AJ, 120, 2868
Winn, J. N., Lovell, J. E. J., Chen, H.-W., et al. 2002a, ApJ, 564, 143
Winn, J. N., Morgan, N. D., Hewitt, J. N., et al. 2002b, AJ, 123, 10
Wisotzki, L., Christlieb, N., Liu, M. C., et al. 1999, A&A, 348, L41
Wisotzki, L., Koehler, T., Kayser, R., & Reimers, D. 1993, A&A, 278, L15
Wisotzki, L., Koehler, T., Lopez, S., & Reimers, D. 1996, A&A, 315, L405
Wisotzki, L., Schechter, P. L., Bradt, H. V., Heinmüller, J., & Reimers, D. 2002, A&A, 395, 17
Wisotzki, L., Schechter, P. L., Chen, H.-W., et al. 2004, A&A, 419, L31

Appendix A: Observational data

In the following we provide colour stamps for our 109 lens candidates classified as grade-A or grade-B (Figs. A.1-A.5). We also provide a list of the objects we classify as ring-like galaxies (Table A.1) or as a grade-C lens candidates (Table A.2).

ID	RA	DEC	ID	RA	DEC	ID	RA	DEC	ID	RA	DEC
1	30.7113	-4.1200	70	208.8451	56.5793	139	212.0681	51.7086	207	216.0082	55.7079
2	32.0140	-7.3349	71	208.8577	55.2961	140	212.0702	54.6277	208	216.1492	53.3707
3	32.7019	-11.091	72	208.8897	56.7042	141	212.0781	53.1058	209	216.1771	56.1187
4	32.9684	-10.640	73	208.9984	57.6036	142	212.1310	56.5988	210	216.2110	53.6238
5	33.3126	-4.5772	74	209.1030	54.2619	143	212.1942	52.2143	211	216.3065	57.5956
6	34.0313	-6.8846	75	209.1158	53.3728	144	212.2530	53.6661	212	216.3152	54.6290
7	34.6449	-6.2790	76	209.1330	57.7878	145	212.3300	52.7731	213	216.4620	56.7888
8	35.3084	-9.6229	77	209.1440	53.1748	146	212.3553	55.9526	214	216.6035	54.0957
9	36.2642	-6.6648	78	209.1640	57.7423	147	212.4420	52.1788	215	216.6826	52.8987
10	37.7604	-5.9290	79	209.1907	56.3655	148	212.4687	51.9757	216	216.9283	57.2185
11	132.1819	-2.5873	80	209.2600	57.224	149	212.4777	56.5225	217	217.1591	55.7337
12	132.2712	-2.7720	81	209.2658	53.3428	150	212.6073	56.4597	218	217.2200	55.6851
13	132.5795	-3.1395	82	209.3485	54.5476	151	212.6626	57.4131	219	217.2537	55.4910
14	132.5827	-2.1625	83	209.3499	54.3683	152	212.6708	52.8456	220	217.3800	55.4627
15	132.5857	-4.6938	84	209.4350	56.9008	153	212.8555	55.0499	221	217.4268	53.9160
16	132.6970	-3.9655	85	209.4560	56.9913	154	212.9167	54.0741	222	217.4859	51.7736
17	132.7400	-1.0218	86	209.5048	57.6376	155	212.9404	57.5752	223	217.5249	52.7104
18	132.7620	-4.4793	87	209.6050	56.5502	156	212.9745	55.3304	224	217.5592	56.9327
19	132.9841	-1.9516	88	209.6506	56.1549	157	213.0125	51.3368	225	217.6319	57.7677
20	133.0210	-4.6829	89	209.7750	53.7688	158	213.1040	53.7781	226	217.7050	55.9099
21	133.1227	-1.7640	90	209.8462	56.0677	159	213.1345	52.4077	227	217.8106	57.2403
22	133.1827	-1.0132	91	209.8569	53.1140	160	213.1900	53.6537	228	217.9196	54.5902
23	133.2438	-3.7043	92	210.0242	53.2755	161	213.2580	53.1980	229	218.0436	54.5195
24	133.5939	-4.9943	93	210.0400	54.7716	162	213.2939	57.2640	230	218.0770	54.9706
25	133.6931	-2.7340	94	210.0919	52.5197	163	213.3095	52.4831	231	218.3619	55.3975
26	133.7100	-5.0446	95	210.1264	54.9506	164	213.5020	56.2184	232	218.5645	52.6184
27	133.7260	-3.9403	96	210.2546	52.4485	165	213.5440	57.3132	233	218.6160	57.6086
28	133.7880	-1.4389	97	210.2719	57.5983	166	213.5494	52.3798	234	218.6570	57.5602
29	133.9045	-4.3638	98	210.3997	57.7682	167	213.7320	52.3263	235	218.8210	55.4744
30	133.9124	-2.3331	99	210.4121	53.2592	168	213.7877	53.2259	236	218.8813	54.4891
31	133.9648	-4.7568	100	210.4300	51.2151	169	213.8380	57.1487	237	218.9065	51.3609
32	134.1370	-3.0186	101	210.4339	55.3332	170	213.9270	56.0135	238	219.3108	54.4433
33	134.1507	-1.3852	102	210.4797	51.2445	171	213.9639	51.3241	239	219.4381	56.3716
34	134.2170	-3.9283	103	210.4847	57.6922	172	213.9691	51.9893	240	219.5293	53.7316
35	134.2991	-4.3455	104	210.4876	53.2545	173	213.9950	51.5452	241	219.6096	52.1294
36	134.4163	-2.7038	105	210.4968	55.0219	174	214.0239	57.0921	242	219.6133	52.4955
37	134.4683	-3.6448	106	210.5020	53.1556	175	214.1700	54.0163	243	220.2990	57.7254
38	134.5020	-3.2156	107	210.5154	52.3060	176	214.2040	55.4237	244	330.1120	1.5701
39	134.5101	-3.6909	108	210.6305	51.6363	177	214.4082	57.2170	245	330.2540	3.6684
40	134.5972	-2.1057	109	210.7200	52.8003	178	214.4454	55.4881	246	330.2720	1.8044
41	134.7143	-3.3857	110	210.7309	52.3358	179	214.5368	53.1975	247	330.4520	3.6380
42	134.8220	-4.1856	111	210.7704	53.7681	180	214.6275	56.8027	248	330.5939	1.2562
43	134.9660	-4.5596	112	210.8229	51.8781	181	214.6400	55.6239	249	330.8630	4.4709
44	135.0381	-3.3306	113	210.8282	56.4585	182	214.6506	54.2784	250	330.8980	2.2835
45	135.1403	-3.8596	114	210.9047	53.0148	183	214.6966	56.8438	251	331.3460	1.3502
46	135.3235	-5.5642	115	210.9170	53.8914	184	214.7002	53.3850	252	331.6890	1.0121
47	135.3369	-1.1031	116	211.0441	52.8848	185	214.7420	56.4807	253	331.8380	2.8518
48	135.3720	-1.5786	117	211.0709	57.2175	186	214.8210	56.2483	254	331.9330	2.3048
49	135.5498	-1.4060	118	211.1030	52.1859	187	215.0682	56.3292	255	332.0440	3.5210
50	135.5651	-2.0581	119	211.1110	57.0090	188	215.0730	56.531	256	332.1489	1.9636
51	135.5864	-2.2146	120	211.1478	52.4499	189	215.0828	54.9762	257	332.2340	3.9315
52	135.8341	-1.1346	121	211.2522	52.0962	190	215.2030	56.333	258	332.3800	0.5319
53	135.9001	-2.1360	122	211.2820	56.6721	191	215.2367	52.8727	259	332.6879	1.7517
54	135.9940	-3.2371	123	211.2950	53.9345	192	215.2490	51.4651	260	333.1200	0.8459
55	136.0742	-4.1396	124	211.4487	57.3926	193	215.3003	57.7346	261	333.1270	2.4188
56	136.1734	-2.0613	125	211.5459	56.7882	194	215.3255	57.5031	262	333.1709	0.3183
57	136.2500	-4.7148	126	211.5520	56.0455	195	215.3361	55.3473	263	333.2590	-0.8181
58	136.2506	-2.2494	127	211.6047	51.6347	196	215.3542	57.4317	264	333.4410	0.4691
59	136.3568	-2.6909	128	211.6335	52.0406	197	215.4756	56.7486	265	333.9400	1.5399
60	136.5063	-5.1453	129	211.7230	54.7437	198	215.5070	56.9580	266	334.1099	1.0777
61	136.5580	-1.1363	130	211.7706	54.6133	199	215.6347	54.5268	267	334.3880	1.2319
62	136.5629	-4.7081	131	211.7880	53.3319	200	215.6390	51.7208	268	334.4719	1.3240
63	136.5651	-2.1079	132	211.8378	52.5960	201	215.7157	55.2452	269	334.4760	2.7216
64	136.6360	-4.9990	133	211.8520	54.4707	202	215.8014	57.2830	270	334.6690	-0.4942
65	136.6770	-1.4028	134	211.8555	53.8529	203	215.9419	51.6791	271	335.2009	1.1618
66	136.7488	-1.6531	135	211.8660	54.7334	204	215.9590	51.6543	272	335.2869	0.1860
67	136.7710	-1.2799	136	211.8971	54.1434	205	215.9689	57.2974	273	335.3330	1.0047
68	208.6711	57.7116	137	211.9844	54.6894	206	216.0003	54.6786	274	335.5480	0.5849
69	208.7878	56.4358	138	212.0647	52.3376						

Table A.1. List of ring-like galaxies.

ID	RA	DEC	ID	RA	DEC	ID	RA	DEC	ID	RA	DEC
1	30.7690	-4.3707	47	37.9131	-8.4071	93	210.3239	57.0069	139	213.6360	53.4336
2	31.1471	-6.8370	48	132.6063	-1.6624	94	210.3239	57.0069	140	213.8290	51.5396
3	31.1845	-9.2302	49	132.8670	-1.7824	95	210.3830	52.9747	141	213.8425	54.5827
4	31.1953	-7.4963	50	133.0932	-5.5540	96	210.4185	51.9295	142	213.8930	55.9188
5	31.3286	-9.4541	51	133.1093	-2.1114	97	210.4440	56.0728	143	214.0553	56.3335
6	31.4334	-5.5922	52	133.6085	-3.3218	98	210.4970	55.0210	144	214.1416	54.2238
7	31.4347	-8.9391	53	133.8673	-4.4843	99	210.5960	56.7669	145	214.1440	52.1982
8	31.7222	-6.9676	54	134.1219	-2.8850	100	210.8169	56.3686	146	214.2251	53.2605
9	32.0885	-10.1001	55	134.3641	-3.8366	101	210.8650	54.0454	147	214.4718	56.4726
10	32.1265	-8.6989	56	134.4226	-5.5544	102	210.9850	53.6275	148	214.6783	52.0068
11	32.1489	-10.6963	57	134.9147	-1.7250	103	210.9875	52.7897	149	214.8440	52.0608
12	32.3864	-8.6895	58	135.0480	-4.2772	104	211.0765	56.2987	150	214.8870	55.7473
13	32.5458	-6.9613	59	135.3490	-2.7373	105	211.0960	52.7181	151	214.9260	56.2809
14	32.6089	-4.2655	60	135.3985	-4.6624	106	211.1021	56.0841	152	215.2367	52.8727
15	32.6312	-5.3873	61	135.4108	-4.9603	107	211.2520	52.0962	153	215.5535	52.0773
16	32.7019	-11.0916	62	135.5910	-2.0328	108	211.2966	53.9393	154	215.5858	52.3223
17	32.7654	-10.1586	63	135.7976	-3.1933	109	211.2975	52.6984	155	215.5870	52.5406
18	32.7713	-4.3339	64	135.8190	-1.4759	110	211.4610	56.5435	156	215.9215	53.1101
19	32.7958	-9.1606	65	135.8390	-4.7139	111	211.5791	51.5461	157	216.0830	56.5382
20	32.8151	-4.6442	66	135.8770	-3.3166	112	211.6760	56.8844	158	216.1280	53.7346
21	32.8263	-5.9572	67	135.8916	-4.7350	113	211.7245	54.9516	159	217.1294	53.2367
22	33.1106	-9.1819	68	136.1790	-2.0222	114	211.7933	57.7058	160	217.2020	57.1215
23	33.1371	-8.2071	69	136.3051	-1.7993	115	211.8378	52.5960	161	217.3254	51.2955
24	33.4489	-5.0069	70	136.4287	-4.3918	116	211.8980	54.3523	162	217.3837	57.0770
25	33.7189	-10.2549	71	136.6511	-4.1206	117	211.9132	56.5606	163	217.4874	53.4669
26	33.8125	-7.6329	72	136.6759	-3.4018	118	212.0111	54.5693	164	217.5479	53.9042
27	33.8846	-7.3768	73	136.7700	-3.6983	119	212.3363	53.7088	165	218.5887	53.5343
28	34.0291	-10.4792	74	208.5923	56.9917	120	212.5192	52.8386	166	218.9180	51.5978
29	34.0313	-6.8846	75	209.0410	55.1548	121	212.5344	53.5059	167	218.9306	51.6789
30	34.0420	-4.9278	76	209.0520	55.3643	122	212.5578	57.1932	168	218.9306	51.6789
31	34.2354	-7.3950	77	209.0883	54.6384	123	212.6180	54.6689	169	219.2150	53.1183
32	34.4127	-5.6183	78	209.1308	56.8001	124	212.7260	56.5193	170	219.2270	54.7119
33	34.7033	-6.3146	79	209.3442	56.0257	125	212.7260	54.2777	171	219.2620	53.0397
34	34.7611	-5.6861	80	209.4020	56.8134	126	212.7260	56.5193	172	219.4122	56.8565
35	34.7705	-8.1057	81	209.6070	52.7409	127	212.7370	53.3133	173	219.5995	53.3351
36	35.1727	-10.8737	82	209.6217	52.6670	128	212.8499	56.3970	174	219.6419	54.4867
37	35.4835	-10.6293	83	209.6358	56.3116	129	212.8877	56.1517	175	219.6730	56.9740
38	35.4901	-6.8625	84	209.8516	54.3894	130	212.9065	53.8578	176	331.1035	1.3934
39	35.5342	-8.2175	85	209.9950	56.2114	131	212.9810	52.5545	177	331.8447	4.2985
40	36.0965	-3.9120	86	210.0480	53.4897	132	213.1729	54.4224	178	331.9094	1.6015
41	37.1595	-8.0260	87	210.1192	56.0877	133	213.1870	55.2213	179	332.0385	1.5294
42	37.3517	-11.1634	88	210.1260	54.9506	134	213.3750	53.4311	180	332.0615	2.6110
43	37.3725	-9.9510	89	210.1920	55.5750	135	213.4316	53.0792	181	332.1574	3.3451
44	37.7770	-10.0155	90	210.2130	52.9077	136	213.5034	55.1556	182	332.7543	0.0248
45	37.8688	-9.2495	91	210.2437	56.8107	137	213.5379	52.4758	183	333.8364	0.9369
46	37.9131	-8.4071	92	210.3010	57.0831	138	213.5680	54.4716			

Table A.2. List of our grade-*C* candidates in CFHTLS.

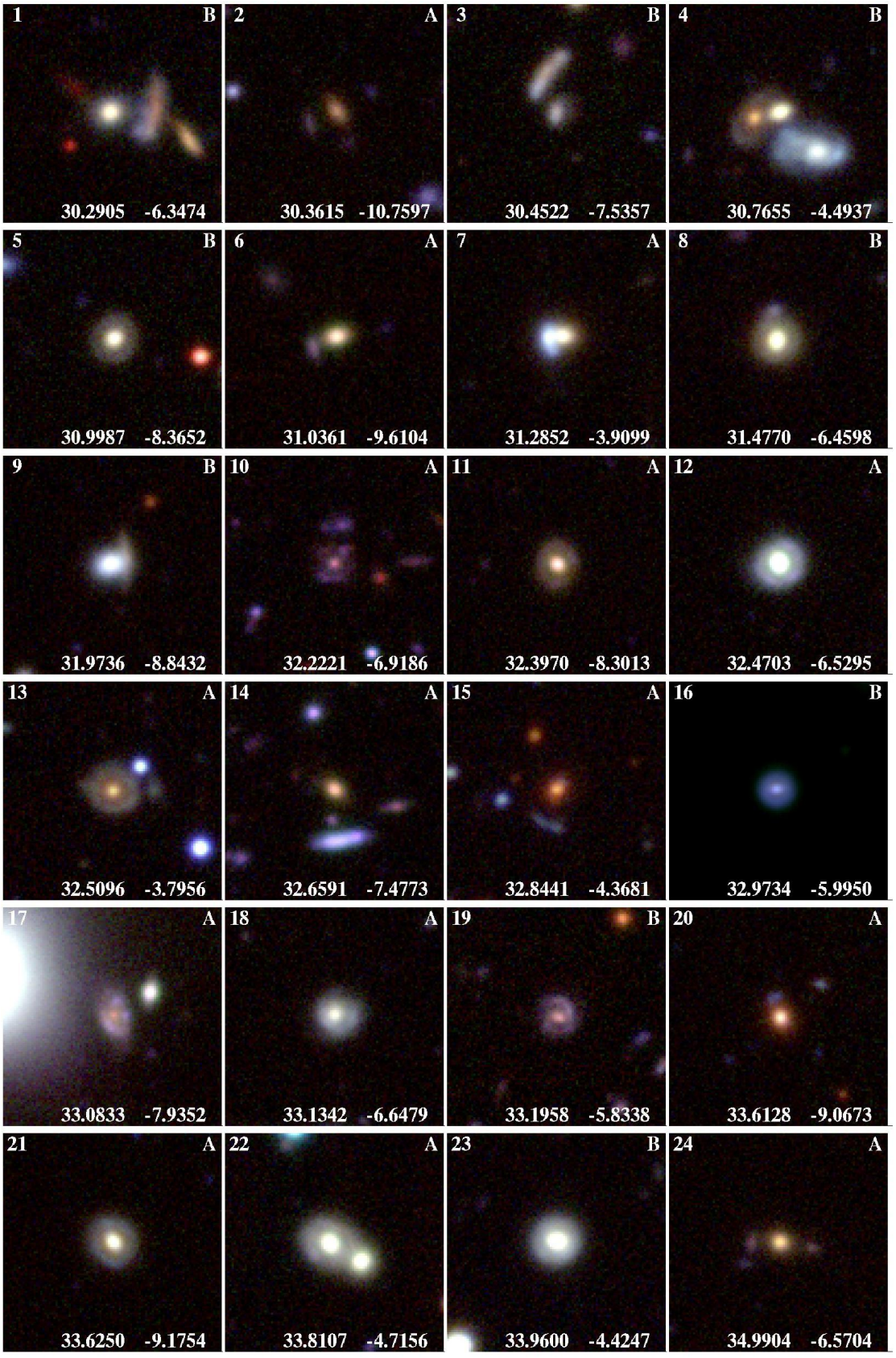

Fig. A.1. Our new lenses found with the PCA-finder, with grades *A* and *B* (see text). The stamps are 18.7″on-a-side.

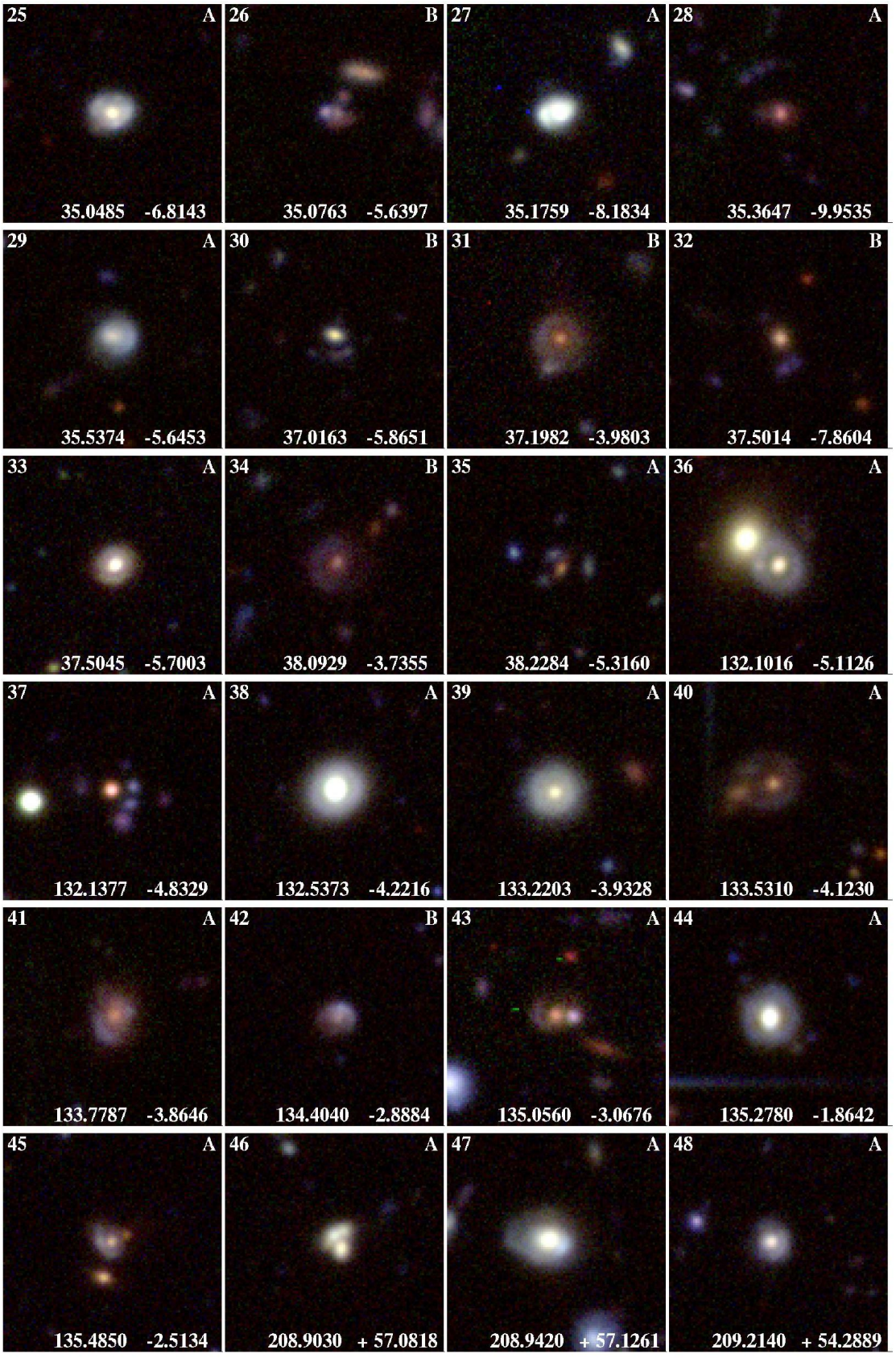

Fig. A.2. Our new lenses found with the PCA-finder, with grades *A* and *B* (see text). The stamps are 18.7″on-a-side.

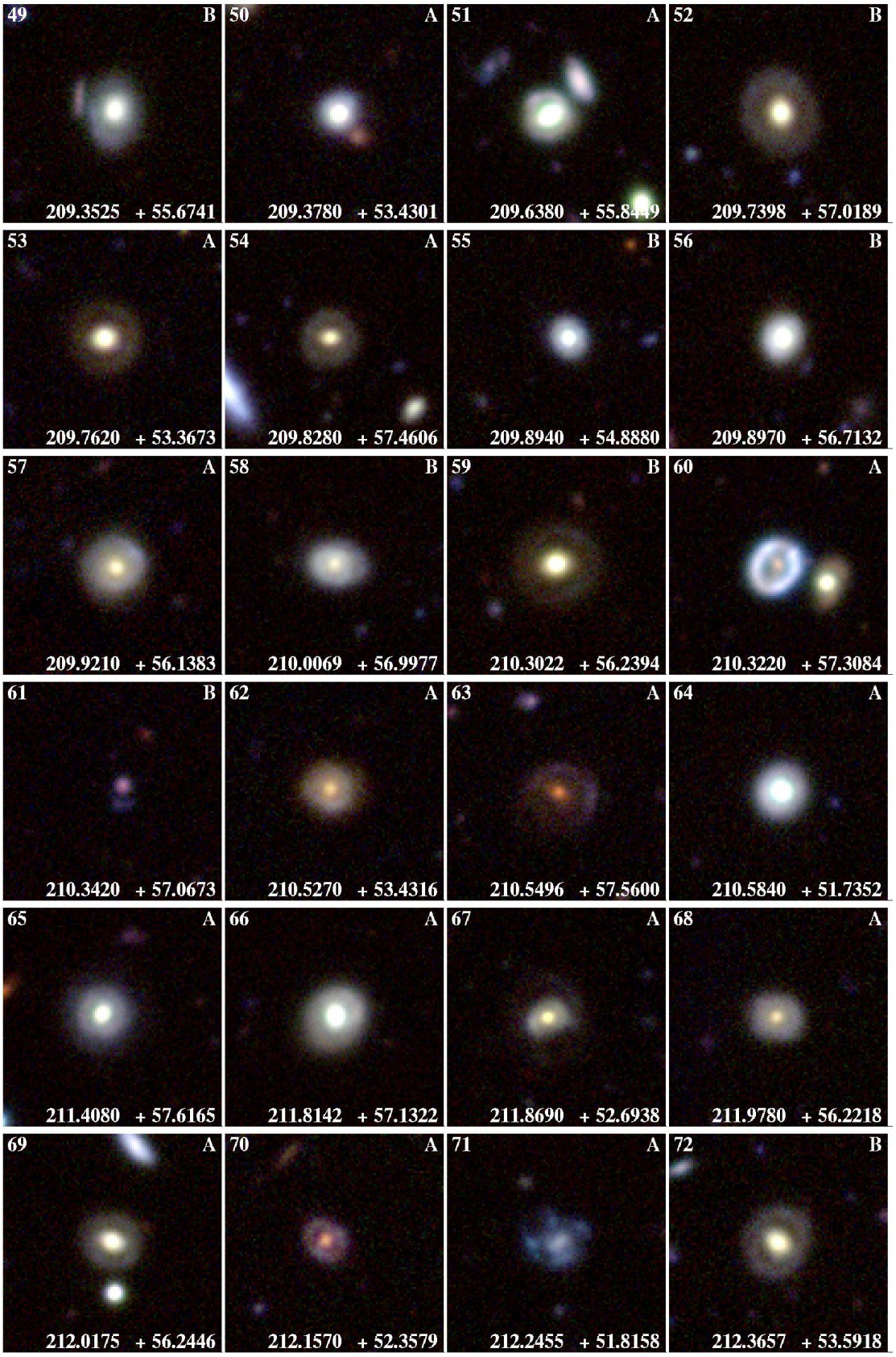

Fig. A.3. Our new lenses found with the PCA-finder, with grades *A* and *B* (see text). The stamps are 18.7″on-a-side.

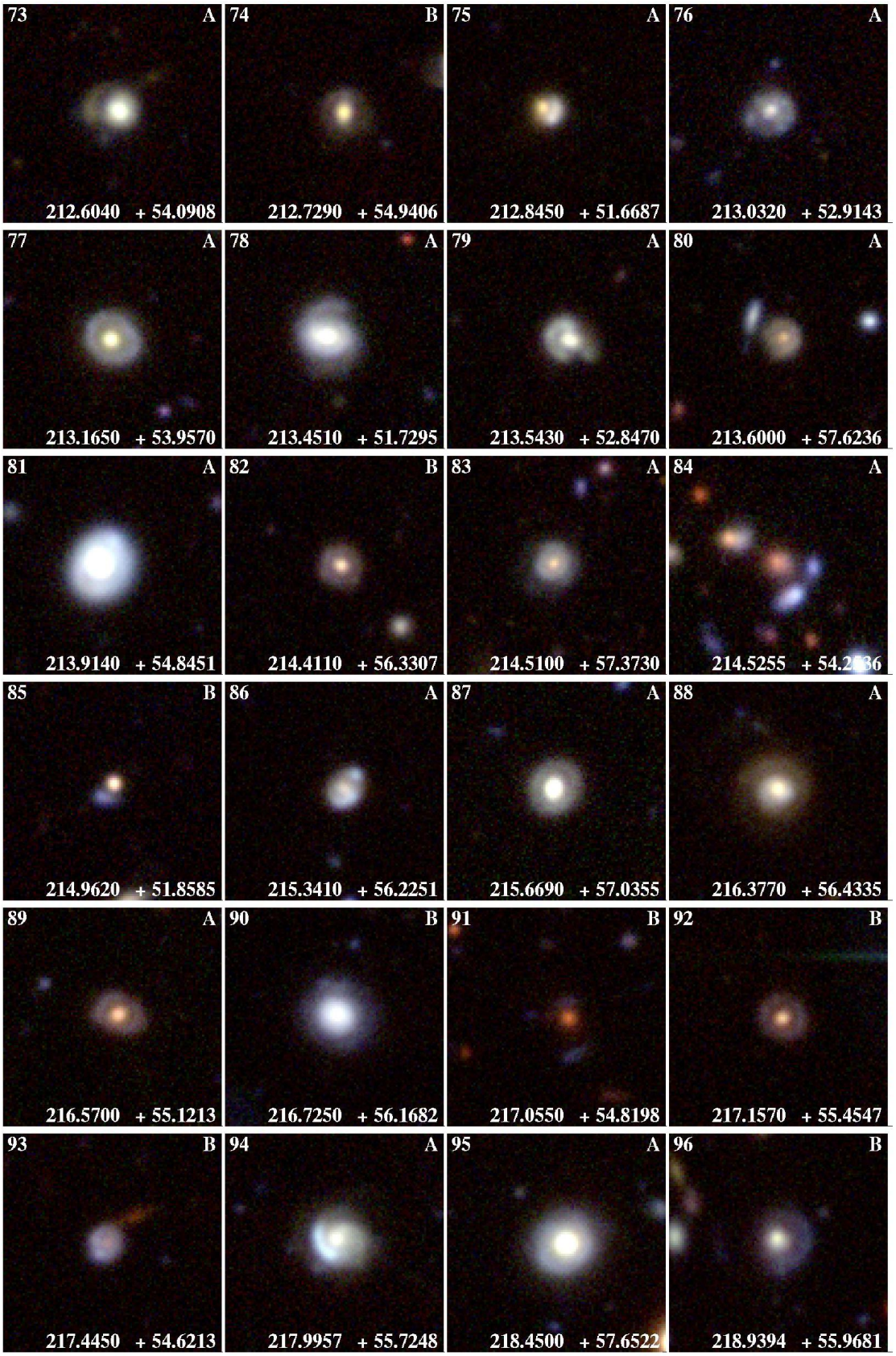

Fig. A.4. Our new lenses found with the PCA-finder, with grades *A* and *B* (see text). The stamps are 18.7″on-a-side.

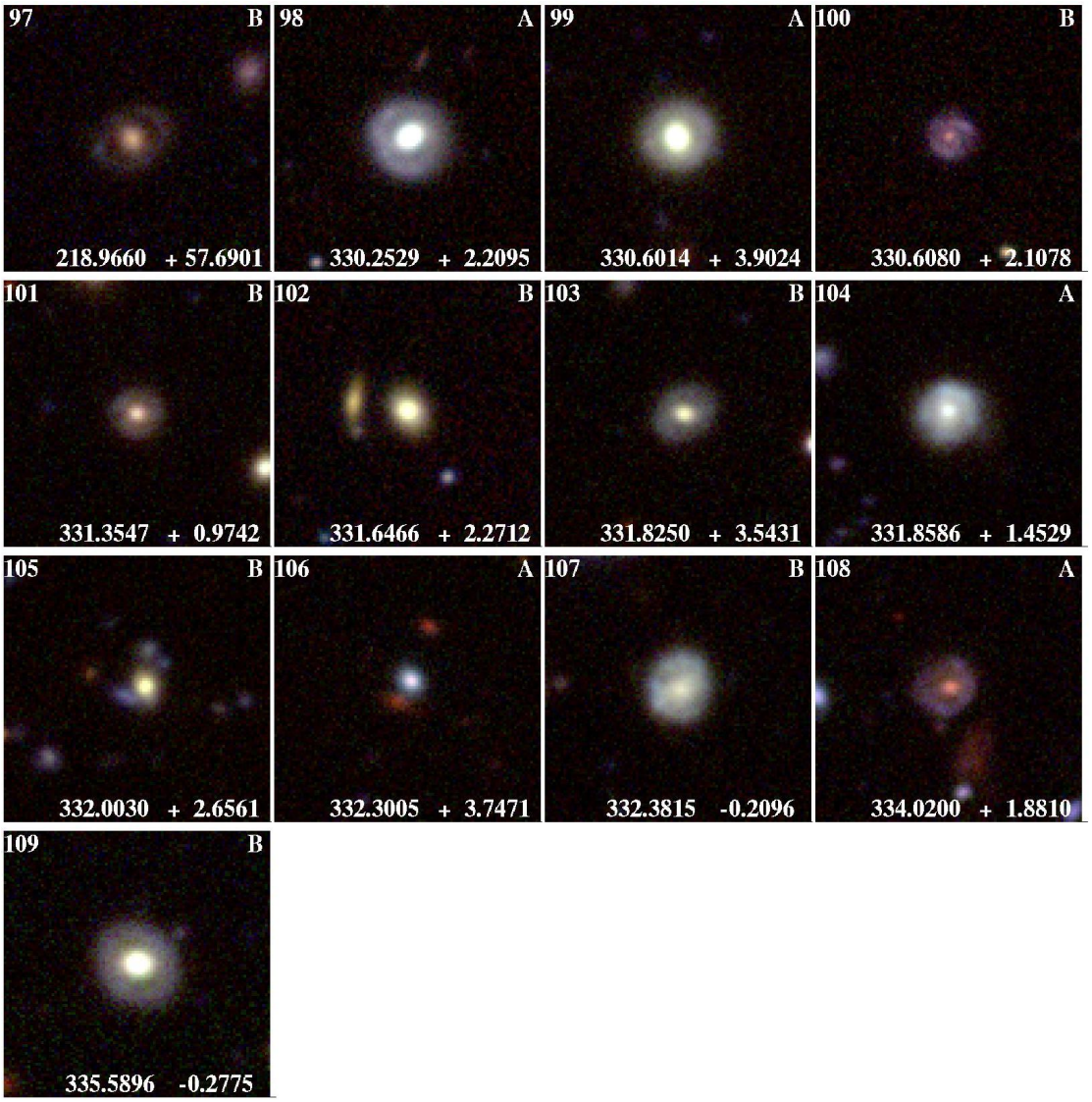

Fig. A.5. Our new lenses found with the PCA-finder, with grades *A* and *B* (see text). The stamps are 18.7″on-a-side.